

Adaptive Smooth Control via Nonsingular Fast Terminal Sliding Modes for Distributed Space Telescope Demonstration Mission by CubeSat Formation Flying

Soobin Jeon

Ph.D Candidate, Department of Astronomy, Yonsei University, Seoul 03722, Republic of Korea

Hancheol Cho

Associate Professor, Department of Astronomy, Yonsei University, Seoul 03722, Republic of Korea
Visiting Assistant Professor, Department of Aerospace Engineering, Embry-Riddle Aeronautical University, Daytona Beach, FL 32114, USA

Sang-Young Park

Professor, Department of Astronomy, Yonsei University, Seoul 03722, Republic of Korea

Abstract— This paper investigates the efficiency of a nonsingular fast terminal sliding mode-based adaptive smooth control method for the distributed space telescope demonstration mission. The distributed space telescope has a flexible focal length that corresponds to the relative position in the formation flying concept. The precise formation flying technology implemented by CubeSats enhances the utility of distributed space systems at low costs. The limited specification of the CubeSat generally restricts the performance of the actuators – most critically the degrees of freedom. Conventional formation flying missions generally aim to verify relative orbit control technologies such as formation keeping and reconfiguration on the orbits that are stable in natural dynamics. The state-of-the-art precise formation flying has developed for more elaborate missions of scientific purposes. One of the scientific formation flying missions is the distributed space telescope that observes a celestial object by aligning two satellites. The reference trajectory of the distributed space telescope is designed to head

Manuscript received XXXXX 00, 0000; revised XXXXX 00, 0000; accepted XXXXX 00, 0000.

Corresponding author: S.-Y. Park

Soobin Jeon is with the Department of Astronomy, Yonsei University, Seoul 03722, Republic of Korea (e-mail: forestine@yonsei.ac.kr). Hancheol Cho is with the Department of Astronomy, Yonsei University, Seoul 03722, Republic of Korea (e-mail: hancho37@yonsei.ac.kr) and the Department of Aerospace Engineering, Embry-Riddle Aeronautical University, Daytona Beach, FL 32114, USA (e-mail: choh15@erau.edu). Sang-Young Park is with the Department of Astronomy, Yonsei University, Seoul 03722, Republic of Korea (e-mail: spark624@yonsei.ac.kr).

0018-9251 © 2023 IEEE

toward an inertial celestial target and is not based on natural dynamics. The characteristics of the reference trajectory for the scientific mission and the restricted specifications of CubeSats induce the attitude and orbit control system to be designed for continuous control and mutually affect the control performance. The nonsingular fast terminal sliding mode proposed in this study has the advantage of a fast convergence rate and is able to improve the control performance. The adaptive smooth controller previously designed for a single-input single-output system is extended and applied to the attitude and orbit control system as an example of a control of a multi-input multi-output system. The simulation results verify the efficiency of the proposed adaptive smooth controller based on the nonsingular fast terminal sliding mode.

Index Terms— Robust control, Nonsingular fast terminal sliding mode control, Adaptive control, CubeSat, Formation flying

Nomenclature

$\mathbf{r} = [x \ y \ z]^T$	Relative position vector in the LVLH frame
$\dot{\mathbf{r}} = [\dot{x} \ \dot{y} \ \dot{z}]^T$	Relative velocity vector in the LVLH frame
$\mathbf{q} = [q_v^T \ q_s]^T$	Quaternion
m	Mass of the deputy satellite, kg
$(\cdot)^i$	A variable or parameter in an inertial frame
$(\cdot)^l$	A variable or parameter in the LVLH frame
$(\cdot)^b$	A variable or parameter in the body frame
$(\cdot)_c$	A variable or parameter of the chief satellite
$(\cdot)_d$	A variable or parameter of the deputy satellite
$(\cdot)_{att}$	A variable or parameter of the attitude control system
$(\cdot)_{orb}$	A variable or parameter of the relative orbit control system
$(\cdot)_r$	Reference, desired, or target variable or parameter
$(\cdot)_e$	Error variable or parameter

I. Introduction

The advancement of satellite development technology has led to the concept of a distributed space system, which aims to substitute medium or large single satellites with a number of small satellites [1]–[3]. The distributed space system is a system that integrates several satellites into a single architecture and encompasses satellite constellations, formation flying, and distributed space telescopes, etc. Distributed space systems offer the capability that strategically organizes the configuration of satellites in accordance with given mission objectives. Hence, it contributes to expand the diversity and flexibility of scientific missions utilizing satellites.

The conventional formation flight missions have reference relative trajectories that are designed based on the relative dynamics exhibited by two similar satellites. Therefore, the reference trajectory retains its stability in

the absence of a control input. The Gravity Recovery and Climate Experiment (GRACE) and the Gravity Recovery and Climate Experiment Follow-on (GRACE-FO) mission is a scientific mission that quantifies the gravitational field by analyzing alterations in relative motion [4], [5]. TerraSAR-X/TanDEM-X (TSX/TDX) satellites acquire ground observation data regularly by applying instantaneous thrust to maintain relative motion within the control window [6]. The formation flight control technology verification mission either modifies the relative orbit to rendezvous (CanX-4/5) or executes inter-satellite docking with proximity operations (CPOD) [7]–[9].

A distributed space telescope is a kind of distributed space system that observes inertial objects by formation flying of dual-spacecraft. The distributed space telescope that is also known as the binary-distributed telescope [10] or the virtual telescope (VT) [11] refers to a group of multiple satellites equipped with optics and detection payload functions as a single instrument [10]. Distributed telescopes have a variable and extensive local length compared to monolithic telescopes and consist of a number of more compact structures, which has the advantage of relatively low launch and development costs [12]. This paper uses the term distributed space telescope.

Inertial Alignment Hold (IAH) is the technology that maintains a specific configuration for the inertial target in order to implement distributed space telescopes. The relative distance of the formation flying is the telescope's baseline or focal length and is designed to range from 1,000 to 72,000 kilometers (astrophysical targets) [13], [14] to 50 to 500 meters (heliophysical targets and X-ray images) [15], [16], depending on the observation target and wavelength band. In contrast to conventional formation flight missions, the reference trajectories of the inertial alignment hold missions should be designed with the separation of focal lengths with respect to the inertial targets. Since the control law must retain the alignment precisely within the requirements, this paper suggests a robust control approach that compensates for the effects of disturbances using continuous thrust.

The main factors that contribute to disturbances in space are uncertainties in the structural properties and unmodeled perturbation forces [17]. The robust system should be able to resist these effects that are neglected in the design phase while performing the tasks. Several robust control techniques have been proposed and have proven their effectiveness in a variety of practical control problems. One common solution for achieving robustness is sliding mode control (SMC) [18]–[20]. The sliding mode control approach allows the system's states to defy the natural motion and follow the designed trajectory, the so-called 'sliding surface.'

The feasibility of the sliding mode control in formation flying missions has been proven in literature over several decades. The adaptive linear and nonsingular terminal sliding mode control approach achieved submillimeter formation keeping precision even when the operational faults are detected [21]. The continuous

and high-order sliding mode controller with consecutive pulse-width modulation was applied to the satellite formation flying in [22]. The sliding mode approach in this application showed high tracking accuracy in the presence of bounded and matched disturbances and uncertainties. The fuzzy-SMC-based technique successfully conducted reconfiguration within a short time span with a minimum control effort for the multiple satellite formation flying problems [23].

The quaternion-based finite-time control technique with a linear sliding surface and nonlinear control law showed a fast convergence rate and the alleviation of chattering in the attitude synchronization and stabilization problem [24]. The robust sliding mode controller shows its efficiency in electromagnetic formation flight (EMFF) control problems under highly nonlinear environments such as the electromagnetic model and magnetic model uncertainties [25], [26]. In [25], the terminal sliding mode for the relative translational dynamics showed improved performance compared to the linear sliding surface. Another paper [26] applied a linear sliding surface to the relative position and attitude tracking problems and successfully handled the control difficulties of EMFF in close proximity.

In this paper novel nonsingular fast terminal sliding variables for both relative orbit and attitude control systems are designed and their stability is proven based on the Lyapunov theory. The robust smooth adaptive control law compensates for the nonlinearity of the relative orbit and attitude systems. The sliding variable and adaptive control law are verified with high fidelity by applying them to a real CubeSat Formation Flying mission launched in 2021 to demonstrate a distributed space telescope. The paper also suggests the performance metrics to describe the characteristics of the control systems.

The first section describes the historical background of the distributed space telescope and sliding mode control, the contribution of this paper sequentially. Section II describes the concept and the characteristics of the Guidance, Navigation, and Control (GN&C) subsystem of the DST demonstration mission by CubeSats. Based on the mission objectives, the reference relative orbit and attitude control systems are defined. The orbit and attitude control systems are both necessary for a precise formation flying (PFF) system, so the dynamic and kinematic equations for the nominal and error states are suggested in Section III. Section IV suggests the sliding variable and robust adaptive control law that are designed based on Lyapunov theory. The control performance for stabilization and tracking problems are described in Section V, which verifies the feasibility of the nonsingular terminal sliding mode controls for the CubeSat formation flying mission developed in this paper. Finally, Section VI concludes the paper.

II. Mission Description

CANYVAL-C Mission

The CANYVAL (CubeSat Astronomy by NASA and Yonsei using the Virtual ALIGNment) project is a distributed space telescope demonstration mission by the formation flying of 1U and 2U CubeSats and was developed by Yonsei University and National Aeronautics and Space Administration (NASA). The 1U satellite is a DSC (Detector Spacecraft) equipped with a visible wavelength camera, and an OSC (Optics Spacecraft), 2U satellite, is equipped with an occulter and it operates the propulsion system to perform orbit control. The nonlinear equation of the relative motion that regards the Earth as a point mass describes the relative states between 1U as the chief and 2U as the deputy.

The configuration based on the mission concept is described in Fig. 1. The first phase of the CANYVAL project is CANYVAL-X (CANYVAL-eXperimental) launched in 2018, and the OSC controls only the alignment angle (θ_{align}) in Fig. 1 so that it has a flexible separation between DSC and OSC [27]. The second phase of the CANYVAL project is CANYVAL-C (CANYVAL-Coronagraph) launched in 2021, and the thruster has a greater degree of freedom to implement the distributed space telescope with a fixed distance of 40 meters [28]. Therefore the formation flying system controls the errors between the relative position of OSC (\mathbf{r}) and the desired trajectory (\mathbf{r}_r) to complete the DSC – OSC – Sun configuration.

Fig. 2 describes the location and orientation of the payload and propulsion system. The CANYVAL-C mission's propulsion system utilizes GomSpace's Nanoprop, which fires cold gas through four nozzles in the $\pm\hat{\mathbf{b}}_x$ and $\pm\hat{\mathbf{b}}_y$ directions of the body fixed frame. The occulter is located and points the $-\hat{\mathbf{b}}_z$ that is normal to the thrust nozzles and it constrains the controllable directions in the local-vertical, local-horizontal (LVLH) frame during alignment to the sun. The propulsion system controls only the satellite's orbit, while the attitude is controlled by

a reaction wheel assembly composed of three reaction wheels. The orbit and attitude control accuracies are dependent on each other because the precise formation flying mission is executed with the use of continuous thrust of the propulsion system with two degrees of freedom.

Mission Objectives

The operational orbit is a sun-synchronous orbit (SSO), and the local time of the ascending node (LTAN) is 11:00. Since the sun-synchronous orbit is circular, the eccentricity of the chief's orbit is assumed to be zero for the mathematical expressions and derivation in section III. The inertial alignment hold consists of the staging and alignment modes for efficient operation [46]. The satellite in the staging mode is reconfigured into an Along-track orbit (ATO) of the along-track distance that corresponds to the focal length of DST. Since the focal length of this mission is 40 meters, the initial state of the alignment mode is designed to be the ATO of a 40-meter distance. Immediately after sunrise, the deputy commences the alignment mode for the extended observation of the sun. In the alignment mode, the deputy aligns toward the sun in the LVLH frame. Therefore the reference trajectory is derived as:

$$\mathbf{r}_r(t) = 40 \cdot \frac{\mathbf{r}_\odot(t)}{\|\mathbf{r}_\odot(t)\|} \quad (\text{m}) \quad (1)$$

where $\mathbf{r}_\odot(t)$ is the sun vector that orients from 1U to the sun and is described in the LVLH frame.

Fig. 3 describes the reference orbital trajectories in the LVLH frame. The reference trajectory of the staging mode is expressed as a cross mark in Fig. 3. On the other hand, the epoch time and LTAN determine the reference trajectory of the alignment mode because it depends on the position of the sun by (1). Fig. 3 shows the reference trajectory of LTAN 11:00 at the vernal equinox

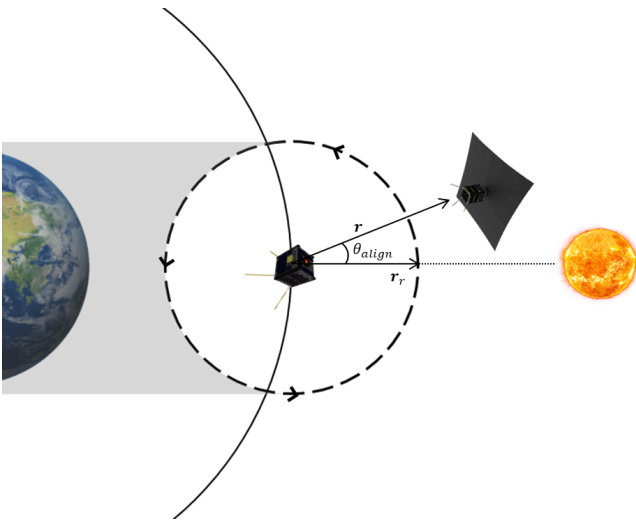


Fig. 1. Distributed space telescope configuration to demonstrate the solar coronagraph

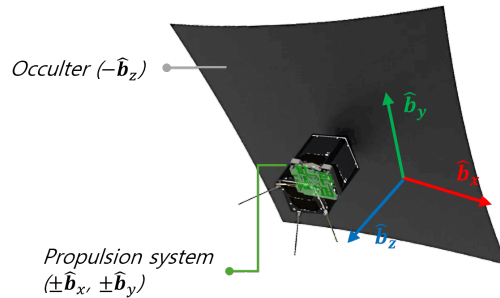


Fig. 2. Location and orientation of the occulter and propulsion system in body frame.

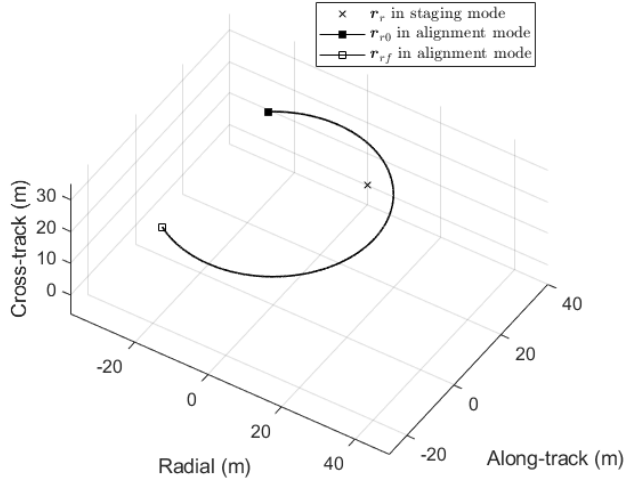


Fig. 3. Reference trajectories described in LVLH frame (cross mark: the reference state in staging mode, filled and empty square: the initial and final reference states in alignment mode, solid line: the reference trajectory in alignment mode)

in which the satellites were planned to be operated for the CANYVAL-C mission.

The reference attitude is derived from the TRIAD algorithm that defines a coordinate frame with two vectors described in the reference and body frames [29], [30]:

$$\mathbf{C}^b \cdot (\mathbf{C}^i)^T = \mathbf{C}_i^b \quad (2)$$

where the superscript b, i of the direction cosine matrix \mathbf{C} refers to the body and reference frame, respectively. Given the two vectors \mathbf{r}_p and \mathbf{r}_s , the direction cosine matrix is derived as

$$\mathbf{C} = [\hat{\mathbf{r}}_1 \quad \hat{\mathbf{r}}_2 \quad \hat{\mathbf{r}}_3] \quad (3)$$

where $\hat{\mathbf{r}}_1 = \mathbf{r}_p / \|\mathbf{r}_p\|$, $\hat{\mathbf{r}}_2 = \mathbf{r}_p \times \mathbf{r}_s / \|\mathbf{r}_p \times \mathbf{r}_s\|$, and $\hat{\mathbf{r}}_3 = \mathbf{r}_p \times (\mathbf{r}_p \times \mathbf{r}_s) / \|\mathbf{r}_p \times (\mathbf{r}_p \times \mathbf{r}_s)\|$.

The quaternion that is also known as the Euler parameters is defined by

$$\mathbf{q}_v = \mathbf{a} \sin(\theta/2), \quad q_4 = \cos(\theta/2) \quad (4)$$

where \mathbf{a} and θ are the Euler axis and the rotation angle about the Euler axis [31], [32].

If q_4 is not zero, the quaternion is able to be derived from the direction cosine matrix as follows [31], [32]:

$$\mathbf{q}_v = \frac{1}{4q_4} [C_{23} - C_{32} \quad C_{31} - C_{13} \quad C_{12} - C_{21}]^T \quad (5)$$

$$q_4 = \frac{1}{2} (1 + C_{11} + C_{22} + C_{33})^{\frac{1}{2}} \quad (6)$$

where $\mathbf{C} = [C_{ij}]$.

The primary vector of the attitude control in the alignment mode is to orient the occulter toward the sun. Since the propulsion system has nozzles only along the x and y directions in the body frame, it rotates 10 degrees with respect to the y direction as an ad-hoc strategy.

Therefore, the vectors that define the reference attitude frame during the alignment mode are:

$$\mathbf{r}_p^i = \mathbf{r}_{\odot}^i, \quad \mathbf{r}_s^i = \mathbf{C}_l^i \cdot [0 \quad 0 \quad 1]^T \quad (7)$$

$$\mathbf{r}_p^b = [0 \quad \pm \sin \theta \quad -1 - \cos \theta]^T \quad (8)$$

$$\mathbf{r}_s^b = [1 \quad 0 \quad 0]^T \quad (9)$$

where \mathbf{C}_l^i is the rotation matrix from the LVLH frame to the inertial frame, θ is the rotation angle that is set as 10 degrees, and the plus sign of \mathbf{r}_p^b indicates that the y and z components of the thrust vector have the same sign. The secondary vectors in the inertial and body frames are derived from the angle β of the sun-synchronous orbit that is the angle between the orbital plane and the sun vector. If the LTAN is supposed to be around 12:00, any normal direction of \mathbf{r}_p^b is recommended to point to the cross-track direction.

The deputy should be located within a sphere of a 3-meter radius to image the solar corona and determine the mission's success [28], [46]. The occulter should point the sun under the three-degree error to shade the sunlight in the image [28], [47]. As a result, the requirements of ROCS and ACS are summarized as follows:

$$\|\mathbf{r} - \mathbf{r}_r\|_2 \leq 3 \quad (\text{m}) \quad (10)$$

$$\theta_e \leq 3 \quad (\text{deg}) \quad (11)$$

where θ_e is the Euler angle of the error quaternion that will be defined in (23).

III. Description of Formation Flying System

This paper assumes that the propulsion system has two degrees of freedom and controls only the orbital states, and the ACS (Attitude Control System) consists of reaction wheels and magnetorquers. Therefore, the attitude actuator controls the body frame so that the resultant fired thrust vector is aligned with the reference thrust vector in advance of the orbital actuator's firing. The relative orbital dynamics is described in the LVLH coordinate system, defined based on point mass gravity. The quaternions and angular velocity represent the attitude and the dynamic models and the dynamic equation includes the rotational motion of the reaction wheels.

A. Relative Orbit Control System

The Keplerian two-body equations of motion of the chief satellite are given by [33]

$$\ddot{\mathbf{r}}_c(t) = -\frac{\mu \mathbf{r}_c(t)}{r_c^3} \quad (12)$$

where $\mathbf{r}_c(t) = [X_c(t) \quad Y_c(t) \quad Z_c(t)]^T$ is the chief's position in the inertial frame with the magnitude of r_c and μ is the standard gravitational parameter of the Earth.

The relative position and the acceleration of the deputy satellite with respect to the chief are defined as

$$\mathbf{r}(t) = \mathbf{r}_d(t) - \mathbf{r}_c(t) \quad (13)$$

$$\begin{aligned}\ddot{\mathbf{r}}(t) &= \ddot{\mathbf{r}}_d(t) - \ddot{\mathbf{r}}_c(t) \\ &= -\frac{\mu(\mathbf{r}(t) + \mathbf{r}_c(t))}{\|\mathbf{r}(t) + \mathbf{r}_c(t)\|_2^3} + \frac{\mu\mathbf{r}_c(t)}{r_c^3}\end{aligned}\quad (14)$$

where $\mathbf{r}_d(t) = [X_d(t) \ Y_d(t) \ Z_d(t)]^T$ is the inertial position of the deputy satellite with the distance from the center of the earth r_d .

The second time derivative of the position vector in the LVLH frame (l) relative to the inertial frame (i) is described in [33], [34] as

$$\begin{aligned}\ddot{\mathbf{r}}(t) &= {}^l \left(\frac{d^2 \mathbf{r}(t)}{dt^2} \right) + 2 {}^i \boldsymbol{\omega}^l \times {}^l \left(\frac{d\mathbf{r}(t)}{dt} \right) \\ &+ \frac{d {}^i \boldsymbol{\omega}^l}{dt} \times \mathbf{r}(t) + {}^i \boldsymbol{\omega}^l \times ({}^i \boldsymbol{\omega}^l \times \mathbf{r}(t))\end{aligned}\quad (15)$$

where ${}^i \boldsymbol{\omega}^l$ is the angular velocity vector of the frame l with respect to the frame i . It is defined as ${}^i \boldsymbol{\omega}^l = [0 \ 0 \ \dot{\theta}_c]^T$ due to its normality to the orbital plane where $\dot{\theta}_c$ is chief's the orbital angular speed.

Therefore, the relative equations of motion are derived as

$$\begin{aligned}\ddot{\mathbf{r}}(t) &= \mathbf{A}_1(\mathbf{r}_c, \dot{\mathbf{r}}_c, \mathbf{r}_d) \mathbf{r}(t) + \mathbf{A}_2(\mathbf{r}_c, \dot{\mathbf{r}}_c) \dot{\mathbf{r}}(t) \\ &+ \mathbf{f}(\mathbf{r}_c, \mathbf{r}_d) + \frac{1}{m} \mathbf{B}(\mathbf{u}_{orb}(t) + \mathbf{d}_{orb}(t, m, \mathbf{r}_d, \dot{\mathbf{r}}_d))\end{aligned}\quad (16)$$

where the nonlinearity of the Keplerian motion $\mathbf{f}(\mathbf{r}_c, \mathbf{r}_d)$, the matrices $\mathbf{A}_1(\mathbf{r}_c, \dot{\mathbf{r}}_c, \mathbf{r}_d)$, $\mathbf{A}_2(\mathbf{r}_c, \dot{\mathbf{r}}_c, \mathbf{r}_d)$, and \mathbf{B} are defined as

$$\begin{aligned}\mathbf{A}_1(\mathbf{r}_c, \dot{\mathbf{r}}_c, \mathbf{r}_d) &= \begin{bmatrix} \dot{\theta}_c^2 - \frac{\mu}{r_d^3} & \ddot{\theta}_c & 0 \\ -\ddot{\theta}_c & \dot{\theta}_c^2 - \frac{\mu}{r_d^3} & 0 \\ 0 & 0 & -\frac{\mu}{r_d^3} \end{bmatrix}, \\ \mathbf{A}_2(\mathbf{r}_c, \dot{\mathbf{r}}_c) &= \begin{bmatrix} 0 & 2\dot{\theta}_c & 0 \\ -2\dot{\theta}_c & 0 & 0 \\ 0 & 0 & 0 \end{bmatrix}, \\ \mathbf{f}(\mathbf{r}_c, \mathbf{r}_d) &= \begin{bmatrix} \frac{\mu}{r_c^2} - \frac{\mu r_c}{r_d^3} \\ 0 \\ 0 \end{bmatrix}, \quad \mathbf{B} = \begin{bmatrix} 1 & 0 & 0 \\ 0 & 1 & 0 \\ 0 & 0 & 1 \end{bmatrix}\end{aligned}\quad (17)$$

and m is the mass of the deputy, θ_c is the true anomaly of the chief, $\mathbf{u}_{orb}(t) = [u_{orb,x}(t) \ u_{orb,y}(t) \ u_{orb,z}(t)]^T$ is the orbital control input, and $\mathbf{d}_{orb}(t, m, \mathbf{r}_d, \dot{\mathbf{r}}_d) = [d_{orb,x} \ d_{orb,y} \ d_{orb,z}]^T$ is the external disturbance force and its three elements have the same arguments but not written here for brevity. The mass m is assumed to have uncertainty as described in Section IV.

Let the tracking error for the relative orbital states be defined by subtracting the reference state $\mathbf{r}_r(t)$ from the current state $\mathbf{r}(t)$:

$$\begin{aligned}\mathbf{r}_e(t) &= \mathbf{r}(t) - \mathbf{r}_r(t) \\ &= [x(t) - x_r(t) \ y(t) - y_r(t) \ z(t) - z_r(t)]^T\end{aligned}\quad (18)$$

where $\mathbf{r}_e(t) = [x_e(t) \ y_e(t) \ z_e(t)]^T$.

Hence, the equations of motion of the orbital errors are derived by substituting (18) into (16) as

$$\begin{aligned}\ddot{\mathbf{r}}_e(t) &= \mathbf{A}_1(\mathbf{r}_c, \dot{\mathbf{r}}_c, \mathbf{r}_d) (\mathbf{r}_e(t) + \mathbf{r}_r(t)) \\ &+ \mathbf{A}_2(\mathbf{r}_c, \dot{\mathbf{r}}_c, \mathbf{r}_d) (\dot{\mathbf{r}}_e(t) + \dot{\mathbf{r}}_r(t)) \\ &+ \mathbf{f}(\mathbf{r}_c, \mathbf{r}_d) + \frac{1}{m} \mathbf{B}(\mathbf{u}_{orb}(t) + \mathbf{d}_{orb}(t, m, \mathbf{r}_d, \dot{\mathbf{r}}_d)) - \ddot{\mathbf{r}}_r(t)\end{aligned}\quad (19)$$

where $\dot{\mathbf{r}}_e(t)$ and $\ddot{\mathbf{r}}_e(t)$ are the first and second-time derivatives of the tracking error and $\ddot{\mathbf{r}}_r(t)$ is the second-time derivative of the reference trajectory.

B. Attitude Control System

The kinematic differential equation for the quaternions and the angular velocity that represents the attitude control system of the satellite is written as follows [30]–[32], [35], [36]

$$\begin{aligned}\dot{\mathbf{q}}(t) &= \begin{bmatrix} \dot{q}_v(t) \\ \dot{q}_4(t) \end{bmatrix} \\ &= \frac{1}{2} \begin{bmatrix} q_4(t) \mathbf{I}_{3 \times 3} + \mathbf{q}^\times(t) & \mathbf{q}_v(t) \\ -\mathbf{q}_v^T(t) & q_4(t) \end{bmatrix} \begin{bmatrix} \boldsymbol{\omega}(t) \\ 0 \end{bmatrix}\end{aligned}\quad (20)$$

where the quaternion $\mathbf{q}(t) = [q_v^T(t) \ q_4(t)]^T$ consists of the vector $\mathbf{q}_v(t) = [q_1(t) \ q_2(t) \ q_3(t)]^T$ and scalar q_4 components, $\boldsymbol{\omega}(t) = [\omega_1(t) \ \omega_2(t) \ \omega_3(t)]^T$ is the angular velocity vector, $\mathbf{I}_{3 \times 3}$ is the 3 by 3 identity matrix, and the skew-symmetric matrix \mathbf{q}^\times is defined as

$$\mathbf{q}^\times(t) = \begin{bmatrix} 0 & -q_3(t) & q_2(t) \\ q_3(t) & 0 & -q_1(t) \\ -q_2(t) & q_1(t) & 0 \end{bmatrix}\quad (21)$$

The attitude dynamical equations of motion with the control torque generated by the reaction wheels under the external disturbances can be expressed as

$$\mathbf{J} \dot{\boldsymbol{\omega}}(t) = -\boldsymbol{\omega}(t) \times (\mathbf{J} \boldsymbol{\omega}(t) + \mathbf{J}_w \boldsymbol{\omega}_w(t)) + \mathbf{u}_{att}(t) + \mathbf{d}_{att}(t)\quad (22)$$

where \mathbf{J} and \mathbf{J}_w are the moment of inertia, which \mathbf{J} contains uncertainty and the subscript w refers to the variables related to the reaction wheels, $\mathbf{u}_{att}(t)$ is the control torque and $\mathbf{d}_{att}(t)$ is the external disturbance torque.

The rotation formula from the current body axes to the reference body axes constructs the attitude tracking error quaternion [30]–[32], [35], [36]

$$\begin{aligned}\mathbf{q}_e(t) &= \begin{bmatrix} q_{ev}(t) \\ q_{e4}(t) \end{bmatrix} \\ &= \begin{bmatrix} q_{r4}(t) \mathbf{q}_v(t) - q_4(t) \mathbf{q}_{rv}(t) - \mathbf{q}_{rv}^\times(t) \mathbf{q}_v(t) \\ q_4(t) q_{r4}(t) + \mathbf{q}_{rv}^T(t) \mathbf{q}_v(t) \end{bmatrix}\end{aligned}\quad (23)$$

where $\mathbf{q}_r(t) = [q_{rv}^T(t) \ q_{r4}(t)]^T$ is the reference attitude trajectory and $\mathbf{q}(t) = [q_v^T(t) \ q_4(t)]^T$ is the current attitude.

The angular velocity error is derived as [30]–[32], [35], [36]

$$\boldsymbol{\omega}_e(t) = \boldsymbol{\omega}(t) - \mathbf{C}_r^b(t) \boldsymbol{\omega}_r(t)\quad (24)$$

where $\boldsymbol{\omega}(t) = [\omega_1(t) \ \omega_2(t) \ \omega_3(t)]^T$ is the current angular velocity and $\boldsymbol{\omega}_r(t) = [\omega_{r1}(t) \ \omega_{r2}(t) \ \omega_{r3}(t)]^T$ is the reference angular velocity.

The matrix $\mathbf{C}_r^b(t)$ represents a rotation matrix from the reference to the current frame and can be expressed for the error quaternion as

$$\begin{aligned} \mathbf{C}_r^b(t) &= \left(q_{e4}^2(t) - \mathbf{q}_{ev}^T(t) \mathbf{q}_{ev}(t) \right) \mathbf{I}_{3 \times 3} + 2\mathbf{q}_{ev}(t) \mathbf{q}_{ev}^T(t) \\ &\quad - 2q_{e4}(t) \mathbf{q}_{ev}^\times(t) \end{aligned} \quad (25)$$

where $\|\mathbf{C}_r^b(t)\| = 1$ and the derivative of the rotation matrix can derive the angular rate of the body fixed frame as

$$\dot{\mathbf{C}}_r^b(t) = -\boldsymbol{\omega}_e^\times(t) \mathbf{C}_r^b(t) \quad (26)$$

Hence, the error kinematics and dynamic equations are written as [30]–[32], [35], [36]

$$\begin{aligned} \dot{\mathbf{q}}_e(t) &= \begin{bmatrix} \dot{\mathbf{q}}_{ev}(t) \\ \dot{q}_{e4}(t) \end{bmatrix} \\ &= \frac{1}{2} \begin{bmatrix} q_{e4}(t) \mathbf{I}_{3 \times 3} + \mathbf{q}_{ev}^\times(t) & \mathbf{q}_{ev}(t) \\ -\mathbf{q}_{ev}^T(t) & q_{e4}(t) \end{bmatrix} \begin{bmatrix} \boldsymbol{\omega}_e(t) \\ 0 \end{bmatrix} \end{aligned} \quad (27)$$

$$\begin{aligned} \mathbf{J} \dot{\boldsymbol{\omega}}_e(t) &= -\left(\boldsymbol{\omega}_e(t) + \mathbf{C}_r^b(t) \boldsymbol{\omega}_r(t) \right) \\ &\quad \times \left(\mathbf{J} \left(\boldsymbol{\omega}_e(t) + \mathbf{C}_r^b(t) \boldsymbol{\omega}_r(t) \right) + \mathbf{J}_w \boldsymbol{\omega}_w(t) \right) \\ &\quad + \mathbf{u}_{att}(t) + \mathbf{d}_{att}(t) \\ &\quad + \mathbf{J} \left(\boldsymbol{\omega}_e^\times(t) \mathbf{C}_r^b(t) \boldsymbol{\omega}_r(t) - \mathbf{C}_r^b(t) \dot{\boldsymbol{\omega}}_r(t) \right) \end{aligned} \quad (28)$$

C. Problem Statement

To summarize Sections II and III, the relative orbit control problem of the CANYVAL-C mission is simplified as two applications: stabilization (staging mode) and tracking problem (alignment mode). The objective of this paper is to design a sliding surface and a control law for the formation flying system so that the errors of the relative orbit and attitude achieve zero in finite time, that is:

$$\lim_{t \rightarrow t_{f,1}} (\mathbf{r}(t) - \mathbf{r}_r(t)) = \mathbf{0} \quad (29)$$

$$\lim_{t \rightarrow t_{f,2}} (\dot{\mathbf{r}}(t) - \dot{\mathbf{r}}_r(t)) = \mathbf{0} \quad (30)$$

$$\begin{aligned} \lim_{t \rightarrow t_{f,3}} (q_{r4}(t) \mathbf{q}_v(t) - q_4(t) \mathbf{q}_{rv}(t) \\ - \mathbf{q}_{rv}^\times(t) \mathbf{q}_v(t)) = \mathbf{0} \end{aligned} \quad (31)$$

$$\lim_{t \rightarrow t_{f,4}} \left(\boldsymbol{\omega}(t) - \mathbf{C}_r^b(t) \boldsymbol{\omega}_r(t) \right) = \mathbf{0} \quad (32)$$

where the $t_{f,\{1,2,3,4\}}$ are the finite time that the errors converge to the region and the errors are defined in Section III.

IV. Control System Design

Assumption 1. The state vectors of the satellite $(\mathbf{r}, \dot{\mathbf{r}}, \mathbf{q}_v, \boldsymbol{\omega})$ are measurable and available throughout the spaceflight mission.

Assumption 2. The uncertain structural properties in the orbit and attitude control systems are the mass and moment of inertia that have unknown lower and upper bounds. In this paper, the mass and moment of inertia are supposed to be bounded as

$$m(t) = m_0 + \delta m(t) \quad (33)$$

$$\mathbf{J}(t) = \mathbf{J}_0 + \delta \mathbf{J}(t) \quad (34)$$

where the subscripts ‘0’ and δ denote the nominal (known) and uncertain values of the variable, respectively.

Assumption 3. The external disturbances are perturbations that include the asymmetric gravity of the Earth, atmospheric drag, and solar radiation pressure. They induce disturbance forces and torques but are bounded by unknown values:

$$0 < d_f < \|\mathbf{d}_{orb}(t, m, \mathbf{r}_d, \dot{\mathbf{r}}_d)\|_2 < D_f \quad (35)$$

$$0 < d_\tau < \|\mathbf{d}_{att}(t)\|_2 < D_\tau \quad (36)$$

where (d_f, D_f) and (d_τ, D_τ) are the lower and upper bounds of the orbital and attitude disturbances respectively, and are unknown.

Adaptive control law

The adaptive smooth control law is based on sliding mode control and drives the sliding variable into the user-specified domain without the chattering phenomenon. The control law is proposed for the formation flying control system as follows [37]:

$$\mathbf{u}(t) = -\frac{K(t)}{\varepsilon} \mathbf{s}(t) \quad (37)$$

where $K(t)$ is the time-varying gain that obeys the adaptive law defined in (38), $\mathbf{s}(t)$ is the sliding surface that will be defined later in this section, and ε is a user-specified positive constant.

The gain is updated by the adaptation law proposed in [37] as follows:

$$\dot{K}(t) = \eta (\|\mathbf{u}(t)\|_2 - K(t) + K_0), K(0) \geq K_0 \quad (38)$$

where $\mathbf{u}(t)$ is the adaptive smooth control law in (37), η is a user-specified positive constant, and K_0 is the lower bound of the control gain that is positive and user-specified and $\|\cdot\|_2$ is a vector 2-norm. With this adaptation law, the 2-norm of the sliding variable is bounded by ε .

A. Relative Orbit Control System

Sliding variable design

The sliding variable for the relative orbit control system is designed based on nonsingular fast terminal sliding mode as follows:

$$\mathbf{s}_{orb}(t) = \dot{\mathbf{r}}_e(t) + \boldsymbol{\alpha}_{orb} \text{sig}^{\rho_{orb}} \mathbf{r}_e(t) + \boldsymbol{\beta}_{orb} \mathbf{r}_e(t) \quad (39)$$

where $\rho_{orb} \in (1, 2)$, $\boldsymbol{\alpha}_{orb} = \text{diag} \{ \alpha_{orb,1}, \alpha_{orb,2}, \alpha_{orb,3} \}$, $\boldsymbol{\beta}_{orb} = \text{diag} \{ \beta_{orb,1}, \beta_{orb,2}, \beta_{orb,3} \}$ are user-specified positive constants where $\alpha_{orb,i=1,2,3} >$

0 and $\beta_{orb,i=1,2,3} > 0$. Besides, $\text{sig}^\rho \xi = [|\xi_1|^\rho \text{sgn}(\xi_1) \quad |\xi_2|^\rho \text{sgn}(\xi_2) \quad |\xi_3|^\rho \text{sgn}(\xi_3)]^T$ for a vector $\xi = [\xi_1 \quad \xi_2 \quad \xi_3]^T$. The subscript and arguments of the variables and parameters will be suppressed for brevity unless required.

Lemma 1. *Suppose a continuous positive definite function $V : \mathbb{R}^n \rightarrow \mathbb{R}$ for a continuous system $\dot{\mathbf{x}} = f(\mathbf{x})$, $f(\mathbf{0}) = \mathbf{0}$, and $\mathbf{x} \in \mathbb{R}^n$. The extended Lyapunov finite-time stability description guarantees the stability of the origin as*

$$\dot{V}(\mathbf{x}) + aV(\mathbf{x}) + bV^m(\mathbf{x}) \leq 0, \quad \mathbf{x} \in U_0 \quad (40)$$

where $a \in \mathbb{R}^+$, $b \in \mathbb{R}^+$, $m \in (0, 1)$, and $U_0 \subseteq \mathbb{R}^n$ is an open neighborhood of the origin. The finite convergence time is achieved as

$$t \leq \frac{1}{a(1-m)} \ln \frac{aV^{1-m}(x_0) + b}{b} \quad (41)$$

where $\mathbf{x}(0) = \mathbf{x}_0$ [38].

Proposition 1. *The relative position and velocity errors $(\mathbf{r}_e, \dot{\mathbf{r}}_e)$ are asymptotically stable if the sliding variable s defined in (39) is zero.*

Proof:

Let the Lyapunov candidate be defined as

$$V = \frac{1}{2} \mathbf{r}_e^T \mathbf{r}_e \quad (42)$$

The time derivative of the orbital sliding variable yields

$$\dot{s} = \ddot{\mathbf{r}}_e + \boldsymbol{\alpha} \rho \mathbf{R} \dot{\mathbf{r}}_e + \boldsymbol{\beta} \dot{\mathbf{r}}_e \quad (43)$$

where $\mathbf{R} = \text{diag} \{ |x_e|^{\rho-1}, |y_e|^{\rho-1}, |z_e|^{\rho-1} \}$.

The time derivative is derived as

$$\begin{aligned} \dot{V} &= \mathbf{r}_e^T \dot{\mathbf{r}}_e \\ &= \mathbf{r}_e^T (-\boldsymbol{\alpha} \text{sig}^\rho \mathbf{r}_e - \boldsymbol{\beta} \dot{\mathbf{r}}_e) \\ &\leq \alpha_{\min} \|\mathbf{r}_e\|_2^{\rho+1} + \beta_{\min} \|\mathbf{r}_e\|_2^2 \\ &= -\alpha_{\min} V^{\frac{\rho+1}{2}} - \beta_{\min} V \end{aligned} \quad (44)$$

where $s = \mathbf{0}$ is used, $\alpha_{\min} = \min_{i=1,2,3} \alpha_i$ and $\beta_{\min} = \min_{i=1,2,3} \beta_i$.

Hence when the sliding variable is maintained to be zero, the orbital error states also converge to zero asymptotically by Lemma 1. ■

Lemma 2. *Consider V is a C^1 smooth positive definite function that is defined on $U \subset \mathbb{R}^n$. If $\dot{V} + cV^r$ is a negative semi definite function where $c \in \mathbb{R}^+$ and $r \in (0, 1)$, then there exists a region $U_0 \subset \mathbb{R}^n$ such that V can approach zero in finite time from the initial value V_0 on the region U_0 . The convergence time is known as $t \leq \frac{V_0^{1-r}}{c(1-r)}$ [39]–[43].*

Theorem 1. *Consider the relative orbit control system that is nonlinear and uncertain (16) with the adaptive smooth feedback control (37)–(38) where p in the adaptive law is 2 and the sliding manifold is designed as (39). If $\|s\|_2 > \varepsilon$, then the orbital states converge to the region $\|s\|_2 \leq \varepsilon$ in a finite time.*

Proof:

Let us define the Lyapunov function $V(t)$ as

$$V = \frac{1}{2} \mathbf{s}^T \mathbf{s} + \frac{1}{2\gamma} (K - K^*)^2 \quad (45)$$

where γ and K^* are positive constants and K^* is sufficiently large.

The time derivative is derived as

$$\dot{V} = \mathbf{s}^T \dot{\mathbf{s}} + \frac{1}{\gamma} (K - K^*) \dot{K} \quad (46)$$

Substituting (43) and (19) into (46) yields

$$\begin{aligned} \dot{s} &= \mathbf{A}_1 (\mathbf{r}_e + \mathbf{r}_r) + \mathbf{A}_2 (\dot{\mathbf{r}}_e + \dot{\mathbf{r}}_r) + \mathbf{f} + \frac{1}{m} \mathbf{B} (\mathbf{u} + \mathbf{d}) \\ &\quad - \ddot{\mathbf{r}}_r + \boldsymbol{\alpha} \rho \mathbf{R} \dot{\mathbf{r}}_e + \boldsymbol{\beta} \dot{\mathbf{r}}_e \end{aligned} \quad (47)$$

The terms in (47) are grouped in brackets according to their uncertainties

$$\begin{aligned} \dot{s} &= [\mathbf{A}_1 (\mathbf{r}_e + \mathbf{r}_r) + \mathbf{A}_2 (\dot{\mathbf{r}}_e + \dot{\mathbf{r}}_r) + \mathbf{f} - \ddot{\mathbf{r}}_r + \boldsymbol{\alpha} \rho \mathbf{R} \dot{\mathbf{r}}_e + \boldsymbol{\beta} \dot{\mathbf{r}}_e] \\ &\quad + \frac{1}{m} \mathbf{B} \mathbf{d} + \frac{1}{m} \mathbf{B} \mathbf{u} \end{aligned} \quad (48)$$

With (17), the time derivative of the sliding variable simply leads to

$$\dot{s} = \frac{1}{m} \mathbf{u} + \bar{\mathbf{D}} \quad (49)$$

where $\bar{\mathbf{D}} = [\mathbf{A}_1 (\mathbf{r}_e + \mathbf{r}_r) + \mathbf{A}_2 (\dot{\mathbf{r}}_e + \dot{\mathbf{r}}_r) + \mathbf{f} - \ddot{\mathbf{r}}_r + \boldsymbol{\alpha} \rho \mathbf{R} \dot{\mathbf{r}}_e + \boldsymbol{\beta} \dot{\mathbf{r}}_e] + \frac{1}{m} \mathbf{B} \mathbf{d}$ includes the nonlinearities of the dynamics and uncertainties with the unknown upper bound $\|\bar{\mathbf{D}}\|_2 < \Gamma$. Assume that K^* is selected such that $K^* > m_{\max} \Gamma$ and $K^* > K(t)$ for all time $t \geq 0$ and $K(t)$ is bounded [37], then

$$\begin{aligned} \dot{V} &= \mathbf{s}^T \dot{s} + \frac{1}{\gamma} (K - K^*) \dot{K} \\ &= \mathbf{s}^T \left(\bar{\mathbf{D}} + \frac{1}{m} \mathbf{u} \right) + \frac{1}{\gamma} (K - K^*) \dot{K} \\ &= \mathbf{s}^T \left(\bar{\mathbf{D}} - \frac{K}{m\varepsilon} \mathbf{s} \right) + \frac{1}{\gamma} (K - K^*) \dot{K} \\ &< \|s\|_2 \Gamma - \frac{K}{m\varepsilon} \mathbf{s}^T \mathbf{s} + \frac{1}{\gamma} (K - K^*) \dot{K} \\ &= \frac{\|s\|_2}{m} \left(m\Gamma - \frac{K}{\varepsilon} \|s\|_2 \right) + \frac{1}{\gamma} (K - K^*) \dot{K} \end{aligned} \quad (50)$$

where m_{\max} is the maximum value of the uncertain mass. Let us assume the case where the sliding variable stays in the region $\|s\|_2 > \varepsilon$. Then (50) is derived as

$$\begin{aligned} \dot{V} &< \frac{\|s\|_2}{m} (m\Gamma - K) + \frac{1}{\gamma} (K - K^*) \dot{K} \\ &= \frac{\|s\|_2}{m} (m\Gamma - K^*) + \frac{1}{\gamma} (K - K^*) \dot{K} - \frac{\|s\|_2}{m} (K - K^*) \\ &= \|s\|_2 \left(\Gamma - \frac{K^*}{m} \right) + \frac{1}{\gamma} (K - K^*) \dot{K} - \frac{\|s\|_2}{m} (K - K^*) \\ &< \|s\|_2 \left(\Gamma - \frac{K^*}{m_{\max}} \right) + \frac{1}{\gamma} (K - K^*) \dot{K} - \frac{\|s\|_2}{m} (K - K^*) \\ &= -\lambda_s \|s\|_2 - |K - K^*| \left(-\frac{\|s\|_2}{m} + \frac{1}{\gamma} \dot{K} \right) \end{aligned} \quad (51)$$

where $\lambda_s \triangleq \frac{K^* - m_{max}\Gamma}{m_{max}}$ is defined and the equality condition $K - K^* = -|K - K^*|$ is utilized. Now, a new parameter $\lambda_K > 0$ is introduced such that

$$\begin{aligned} \dot{V} &< -\lambda_s \|s\|_2 - |K - K^*| \left(-\frac{\|s\|_2}{m} + \frac{1}{\gamma} \dot{K} \right) + \lambda_K |K - K^*| \\ &\quad - \lambda_K |K - K^*| \\ &= -\lambda_s \|s\|_2 - |K - K^*| \left(-\frac{\|s\|_2}{m} + \frac{1}{\gamma} \dot{K} - \lambda_K \right) \\ &\quad - \lambda_K |K - K^*| \\ &< -\lambda_s \|s\|_2 - |K - K^*| \left(-\frac{\|s\|_2}{m_{min}} + \frac{1}{\gamma} \dot{K} - \lambda_K \right) \\ &\quad - \lambda_K |K - K^*| \\ &= -\lambda_s \|s\|_2 - \lambda_K |K - K^*| - L \end{aligned} \quad (52)$$

where $L \triangleq |K - K^*| \left(-\frac{\|s\|_2}{m_{min}} + \frac{1}{\gamma} \dot{K} - \lambda_K \right)$. We write (52) as

$$\begin{aligned} \dot{V} &< -\lambda_s \|s\|_2 - \lambda_K |K - K^*| - L \\ &= -\lambda_s \sqrt{2} \cdot \frac{\|s\|_2}{\sqrt{2}} - \lambda_K \sqrt{2\gamma} \cdot \frac{|K - K^*|}{\sqrt{2\gamma}} - L \\ &\leq -\min \left(\lambda_s \sqrt{2}, \lambda_K \sqrt{2\gamma} \right) \cdot \left(\frac{\|s\|_2}{\sqrt{2}} + \frac{|K - K^*|}{\sqrt{2\gamma}} \right) - L \\ &\leq -\lambda \cdot V^{1/2} - L \end{aligned} \quad (53)$$

where $\lambda \triangleq \sqrt{2} \min(\lambda_s, \lambda_K \sqrt{\gamma}) > 0$.

The parameter L could be positive by selecting a proper γ . The positiveness condition $L > 0$ is equivalent to

$$\gamma < \frac{m_{min} \dot{K}}{\lambda_K m_{min} + \|s\|_2} \quad (54)$$

Using (37)-(38) and the conditions $\|s\|_2 > \varepsilon$ and $K \geq K_0$, it can be readily shown that

$$\gamma < \frac{\eta m_{min} K_0}{\lambda_K m_{min} + \varepsilon} \quad (55)$$

If the parameter L is always positive, we can conclude that $\dot{V} < -\lambda V^{1/2} - L < -\lambda V^{1/2}$. Hence the sliding surface converges into the region $\|s\|_2 \leq \varepsilon$ in a finite-time by Lemma 2. ■

Lemma 3. *When the i th element of the orbital sliding variable is bounded by $|s_i(t)| \leq \varepsilon_i$, the bound on the relative position error is bounded as $|r_{ei}(t)| \leq R_i$, where x_e , y_e , and z_e are written as r_{ei} for $i = 1, 2, 3$ respectively to possess the expression of uniformity. R_i is the unique solution of the equation $f(R_i) = 0$, where $f(x) = \varepsilon_i - \alpha_i \text{sig}^\rho x - \beta_i x$.*

Proof:

Let us define the Lyapunov function $V = \frac{1}{2} r_{ei}^2$, then its time derivative is derived as

$$\dot{V} = r_{ei} \dot{r}_{ei} \quad (56)$$

The bound on the sliding surface $|s_i| \leq \varepsilon_i$ constrains \dot{r}_{ei} as

$$g(r_{ei}) \leq \dot{r}_{ei} \leq f(r_{ei}) \quad (57)$$

where $f(x)$ and $g(x)$ are defined as (58) and (59)

$$f(x) = \varepsilon_i - \alpha_i \text{sig}^\rho x - \beta_i x \quad (58)$$

$$g(x) = -\varepsilon_i - \alpha_i \text{sig}^\rho x - \beta_i x \quad (59)$$

The description of $f(x)$ depends on the sign of x and achieves its derivative $\frac{df(x)}{dx}$ as

$$f(x) = \begin{cases} \varepsilon_i + \alpha_i (-x)^\rho + \beta_i (-x) > 0 & \text{if } x < 0, \\ \varepsilon_i > 0 & \text{if } x = 0, \\ \varepsilon_i - \alpha_i x^\rho - \beta_i x & \text{if } x > 0. \end{cases} \quad (60)$$

$$\frac{df(x)}{dx} = -\rho \alpha_i |x|^{\rho-1} - \beta_i < 0 \quad \text{for } \forall x \in \mathbb{R}. \quad (61)$$

Since $f(0) > 0$, $f(x) > 0$ for $\forall x \in \mathbb{R}^-$ and monotonically decreases for $\forall x \in \mathbb{R}$, it is obvious that there exists a unique positive solution $R_{i,p} \in \mathbb{R}^+$ such that $f(R_{i,p}) = 0$. It derives the sign of $f(x)$ is calculated as

$$\begin{cases} f(x) > 0 & \text{for } x < R_{i,p}, \\ f(x) = 0 & \text{for } x = R_{i,p} > 0, \\ f(x) < 0 & \text{for } x > R_{i,p} > 0. \end{cases} \quad (62)$$

On the other hand, $g(x) = f(x) - 2\varepsilon_i$, which means $g(x)$ is translated $f(x)$ along the y direction by $-2\varepsilon_i$.

$$g(x) = \begin{cases} -\varepsilon_i + \alpha_i (-x)^\rho + \beta_i (-x) & \text{if } x < 0, \\ -\varepsilon_i < 0 & \text{if } x = 0, \\ -\varepsilon_i - \alpha_i x^\rho - \beta_i x < 0 & \text{if } x > 0. \end{cases} \quad (63)$$

$$\frac{dg(x)}{dx} = \frac{df(x)}{dx} < 0. \quad (64)$$

Likewise, the sign of $g(x)$ is determined according to $R_{i,n} \in \mathbb{R}^-$ which is the unique solution of $g(R_{i,n}) = 0$.

$$\begin{cases} g(x) > 0 & \text{for } x < R_{i,n} < 0, \\ g(x) = 0 & \text{for } x = R_{i,n} < 0, \\ g(x) < 0 & \text{for } x > R_{i,n}. \end{cases} \quad (65)$$

As a result, substitution of (62), (65) to (57) derives

$$\begin{cases} g(x) \leq \dot{r}_{ei} \leq f(x) < 0 & \text{if } 0 < R_{i,p} < x \\ 0 < g(x) \leq \dot{r}_{ei} \leq f(x) & \text{if } x < R_{i,n} < 0 \end{cases} \quad (66)$$

The parallel translation between $f(x)$ and $g(x)$ derives the relationship between $R_{i,p}$ and $R_{i,n}$ as

$$\begin{aligned} g(R_{i,n}) &= -\varepsilon_i - \alpha_i \text{sig}^\rho R_{i,n} - \beta_i R_{i,n} \\ &= -\varepsilon_i + \alpha_i (-R_{i,n})^\rho + \beta_i (-R_{i,n}) \\ &= f(-R_{i,n}) \\ &= 0 \end{aligned} \quad (67)$$

It suggests that $R_{i,p} = -R_{i,n} = R_i$ because the solutions are unique. The time derivative of the Lyapunov function in (56) become negative when $|r_{ei}| > R_i$ as

$$\dot{V} = r_{ei} \dot{r}_{ei} < 0 \quad (68)$$

which proves that the region $\mathbb{L}_1 = \{r_{ei} \in \mathbb{R} \mid |r_{ei}| \leq R_i\}$ is the domain of attraction. Fig.4 explains this region of attraction as the shaded region satisfies (68). ■

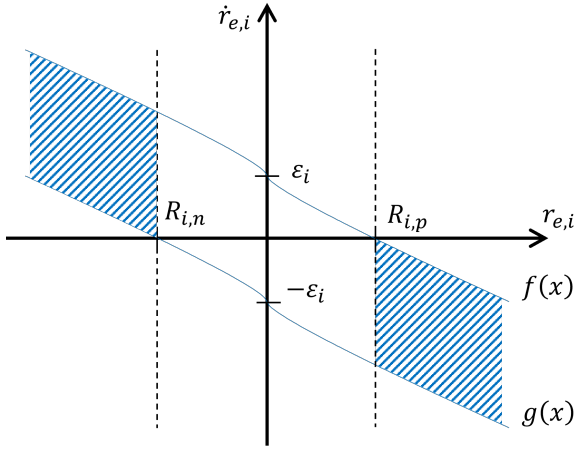


Fig. 4. Bound on r_{ei} in the region $|s_{ei}| \leq \epsilon_i$

B. Attitude Control System

Sliding variable design

The sliding variable for the attitude control system is designed based on nonsingular fast terminal sliding mode as follows:

$$s_{att} = \omega_e + \alpha_{att} \text{sig}^{\rho_{att}} q_{ev} + \beta_{att} q_{ev} \quad (69)$$

where the definition of $\text{sig}^{\rho} \xi$ is the same with the one in (39).

Proposition 2. *The quaternion and angular velocity error (q_{ev}, ω_e) are asymptotically stable if the sliding variable s in (69) is zero.*

Proof:

Let us define the Lyapunov candidate as [44]

$$V = q_{ev}^T q_{ev} + (1 - q_{e4})^2, \quad (70)$$

then the time derivative \dot{V} is derived as

$$\dot{V} = -2\dot{q}_{e4} = q_{ev}^T \omega_e \quad (71)$$

Since the attitude sliding variable is assumed to be zero, then it is derived by substituting (69)

$$\begin{aligned} \dot{V} &\leq q_{ev}^T (-\alpha \text{sig}^{\rho} q_{ev} - \beta q_{ev}) \\ &\leq -\alpha_{min} q_{ev}^T \text{sig}^{\rho} q_{ev} - \beta_{min} q_{ev}^T q_{ev} \\ &\leq -\alpha_{min} \|q_{ev}\|_2^{\rho+1} - \beta_{min} \|q_{ev}\|_2^2 \\ &= -\alpha_{min} V^{\frac{\rho+1}{2}} - \beta_{min} V \end{aligned} \quad (72)$$

where $\alpha_{min} = \min_{i=1,2,3} \alpha_i$ and $\beta_{min} = \min_{i=1,2,3} \beta_i$.

Therefore when the attitude sliding variable is retained at zero, the quaternion error converge to zero. If the sliding variable and the quaternion error are zero, the angular velocity error is also zero according to the definition of the sliding variable in (69). As a result, Lemma 1 proves the finite-time stability of the quaternion and angular velocity errors when the sliding surface is zero. ■

Theorem 2.

Consider the attitude control system that is nonlinear and uncertain (22) with the adaptive smooth feedback control (37) and (38) where p of the adaptive law is 2

and the sliding manifold is designed as (69). If $\|s\|_2 > \epsilon$, then the attitude states converge to the region $\|s\|_2 \leq \epsilon$ in a finite time.

Proof:

The Lyapunov candidate is defined as

$$V = \frac{1}{2} s^T J_0 s + \frac{1}{2\gamma} (K - K^*)^2 \quad (73)$$

where γ is a positive constant and K^* is also a positive constant satisfying $K(t) < K^*$. By the definition of the sliding variable (69), its time derivative is described as

$$\dot{s} = \dot{\omega}_e + (\rho \alpha \Theta + \beta) \dot{q}_{ev} \quad (74)$$

where $\Theta = \text{diag} \{|q_{e1}|^{\rho-1}, |q_{e2}|^{\rho-1}, |q_{e3}|^{\rho-1}\}$ is positive semi-definite.

The momentum of inertia is decomposed as (34), and the inverse matrix is derived as

$$J^{-1} = (J_0 + \delta J)^{-1} = J_0^{-1} + \delta \hat{J} \quad (75)$$

where $\delta \hat{J} = -J_0^{-1} \delta J (I_{3 \times 3} + J_0^{-1} \delta J)^{-1} J_0^{-1}$ by [35], [45].

Hence, the substitution of (75) into (28) leads to the decomposition of the first term in (74) as

$$\begin{aligned} &J^{-1} \left[-(\omega_e + C_r^b \omega_r) \times (J (\omega_e + C_r^b \omega_r) + J_w \omega_w) \right. \\ &\quad \left. + u + d + J (\omega_e^{\times} C_r^b \omega_r - C_r^b \dot{\omega}_r) \right] \\ &= (J_0^{-1} + \delta \hat{J}) \left[-(\omega_e + C_r^b \omega_r) \times (J_0 (\omega_e + C_r^b \omega_r) \right. \\ &\quad \left. + J_w \omega_w) + u + d + (J_0 + \delta J) (\omega_e^{\times} C_r^b \omega_r - C_r^b \dot{\omega}_r) \right] \\ &= J_0^{-1} \left[-(\omega_e + C_r^b \omega_r) \times J_0 (\omega_e + C_r^b \omega_r) \right. \\ &\quad \left. - (\omega_e + C_r^b \omega_r) \times J_w \omega_w + u + J_0 (\omega_e^{\times} C_r^b \omega_r - C_r^b \dot{\omega}_r) \right] \\ &+ J_0^{-1} \left[-(\omega_e + C_r^b \omega_r) \times \delta J (\omega_e + C_r^b \omega_r) \right. \\ &\quad \left. + d + \delta J (\omega_e^{\times} C_r^b \omega_r - C_r^b \dot{\omega}_r) \right] \\ &+ \delta \hat{J} \left[-(\omega_e + C_r^b \omega_r) \times J_0 (\omega_e + C_r^b \omega_r) \right. \\ &\quad \left. - (\omega_e + C_r^b \omega_r) \times \delta J (\omega_e + C_r^b \omega_r) \right. \\ &\quad \left. - (\omega_e + C_r^b \omega_r) \times J_w \omega_w + u + d \right. \\ &\quad \left. + J_0 (\omega_e^{\times} C_r^b \omega_r - C_r^b \dot{\omega}_r) \right. \\ &\quad \left. + \delta J (\omega_e^{\times} C_r^b \omega_r - C_r^b \dot{\omega}_r) \right] \end{aligned} \quad (76)$$

$$\begin{aligned}
&= \mathbf{J}_0^{-1} \mathbf{u} + \mathbf{J}_0^{-1} \left[- \left(\boldsymbol{\omega}_e + \mathbf{C}_r^b \boldsymbol{\omega}_r \right) \times \mathbf{J}_0 \left(\boldsymbol{\omega}_e + \mathbf{C}_r^b \boldsymbol{\omega}_r \right) \right. \\
&\quad \left. - \left(\boldsymbol{\omega}_e + \mathbf{C}_r^b \boldsymbol{\omega}_r \right) \times \mathbf{J}_w \boldsymbol{\omega}_w + \mathbf{J}_0 \left(\boldsymbol{\omega}_e^\times \mathbf{C}_r^b \boldsymbol{\omega}_r - \mathbf{C}_r^b \boldsymbol{\omega}_r \right) \right] \\
&\quad + \mathbf{J}_0^{-1} \left[- \left(\boldsymbol{\omega}_e + \mathbf{C}_r^b \boldsymbol{\omega}_r \right) \times \delta \mathbf{J} \left(\boldsymbol{\omega}_e + \mathbf{C}_r^b \boldsymbol{\omega}_r \right) \right. \\
&\quad \left. + \mathbf{d} + \delta \mathbf{J} \left(\boldsymbol{\omega}_e^\times \mathbf{C}_r^b \boldsymbol{\omega}_r - \mathbf{C}_r^b \boldsymbol{\omega}_r \right) \right] \\
&\quad + \delta \hat{\mathbf{J}} \left[- \left(\boldsymbol{\omega}_e + \mathbf{C}_r^b \boldsymbol{\omega}_r \right) \times \mathbf{J}_0 \left(\boldsymbol{\omega}_e + \mathbf{C}_r^b \boldsymbol{\omega}_r \right) \right. \\
&\quad \left. - \left(\boldsymbol{\omega}_e + \mathbf{C}_r^b \boldsymbol{\omega}_r \right) \times \delta \mathbf{J} \left(\boldsymbol{\omega}_e + \mathbf{C}_r^b \boldsymbol{\omega}_r \right) \right. \\
&\quad \left. - \left(\boldsymbol{\omega}_e + \mathbf{C}_r^b \boldsymbol{\omega}_r \right) \times \mathbf{J}_w \boldsymbol{\omega}_w \right. \\
&\quad \left. + \mathbf{u} + \mathbf{d} + \mathbf{J}_0 \left(\boldsymbol{\omega}_e^\times \mathbf{C}_r^b \boldsymbol{\omega}_r - \mathbf{C}_r^b \boldsymbol{\omega}_r \right) \right] \\
&= \mathbf{J}_0^{-1} \mathbf{u} + \bar{\mathbf{d}}_1 + \bar{\mathbf{d}}_2 + \bar{\mathbf{d}}_3
\end{aligned} \tag{77}$$

where $\bar{\mathbf{d}}_1$, $\bar{\mathbf{d}}_2$, and $\bar{\mathbf{d}}_3$ are the first, second, and third terms of (77).

Therefore, (74) substituted by (27) and (77) is derived as

$$\begin{aligned}
\dot{\mathbf{s}} &= \mathbf{J}_0^{-1} \mathbf{u} + \bar{\mathbf{d}}_1 + \bar{\mathbf{d}}_2 + \bar{\mathbf{d}}_3 \\
&\quad + \frac{1}{2} (\boldsymbol{\rho} \boldsymbol{\alpha} \boldsymbol{\Theta} + \boldsymbol{\beta} \mathbf{I}_{3 \times 3}) (q_{e4} \mathbf{I}_{3 \times 3} + \mathbf{q}_{ev}^\times) \boldsymbol{\omega}_e \\
&= \mathbf{J}_0^{-1} \mathbf{u} + \bar{\mathbf{d}}_1 + \bar{\mathbf{d}}_2 + \bar{\mathbf{d}}_3 + \bar{\mathbf{d}}_4 \\
&= \mathbf{J}_0^{-1} \mathbf{u} + \lambda_{max}^{-1} \bar{\mathbf{d}}
\end{aligned} \tag{78}$$

where $\lambda_{min}^{-1} \bar{\mathbf{d}} = \bar{\mathbf{d}}_1 + \bar{\mathbf{d}}_2 + \bar{\mathbf{d}}_3 + \bar{\mathbf{d}}_4$.

As a result, the time derivative of the Lyapunov function in (73) leads to

$$\begin{aligned}
\dot{V} &= \mathbf{s}^T \mathbf{J}_0 \dot{\mathbf{s}} + \frac{1}{\gamma} (K - K^*) \dot{K} \\
&= \mathbf{s}^T \left(\mathbf{u} + \lambda_{max}^{-1} \mathbf{J}_0 \bar{\mathbf{d}} \right) + \frac{1}{\gamma} (K - K^*) \dot{K} \\
&= \mathbf{s}^T \left(-\frac{K}{\varepsilon} \mathbf{s} + \lambda_{max}^{-1} \mathbf{J}_0 \bar{\mathbf{d}} \right) + \frac{1}{\gamma} (K - K^*) \dot{K} \\
&\leq \lambda_{max}^{-1} \mathbf{s}^T \mathbf{J}_0 \bar{\mathbf{d}} - \frac{K}{\varepsilon} \mathbf{s}^T \mathbf{s} + \frac{1}{\gamma} (K - K^*) \dot{K}
\end{aligned} \tag{79}$$

Since \mathbf{J}_0 is a symmetric matrix, the inequality equation is derived by spectral theorem

$$\mathbf{s}^T \mathbf{J}_0 \bar{\mathbf{d}} \leq \lambda_{max} \|\mathbf{s}\|_2 \|\bar{\mathbf{d}}\|_2 \tag{80}$$

where λ_{max} is the maximum eigenvalue of \mathbf{J}_0 . It follows that

$$\begin{aligned}
\dot{V} &\leq \|\mathbf{s}\|_2 \|\bar{\mathbf{d}}\|_2 - \frac{K}{\varepsilon} \|\mathbf{s}\|_2^2 + \frac{1}{\gamma} (K - K^*) \dot{K} \\
&< \|\mathbf{s}\|_2 \left(D - \frac{K}{\varepsilon} \|\mathbf{s}\|_2 \right) + \frac{1}{\gamma} (K - K^*) \dot{K}
\end{aligned} \tag{81}$$

where $\|\bar{\mathbf{d}}\|_2 < D$. In the region $\|\mathbf{s}\|_2 > \varepsilon$, then

$$\begin{aligned}
\dot{V} &< \|\mathbf{s}\|_2 (D - K) + \frac{1}{\gamma} (K - K^*) \dot{K} \\
&= -\beta_s \|\mathbf{s}\|_2 + \frac{1}{\gamma} (K - K^*) \dot{K}
\end{aligned} \tag{82}$$

where $\beta_s = K - D$ should be positive and it constrains the control gain as $K(t) \geq K_0 > D$.

$$\begin{aligned}
\dot{V} &< -\beta_s \|\mathbf{s}\|_2 - \frac{1}{\gamma} |K - K^*| + \beta_K |K - K^*| - \beta_K |K - K^*| \\
&= -\beta_s \|\mathbf{s}\|_2 - |K - K^*| \left(\frac{1}{\gamma} \dot{K} - \beta_K \right) - \beta_K |K - K^*| \\
&= -\beta_s \|\mathbf{s}\|_2 - \beta_K |K - K^*| - \kappa
\end{aligned} \tag{83}$$

where $K - K^* = -|K - K^*|$ because $K \leq K^*$ and $\kappa \triangleq |K - K^*| \left(\frac{1}{\gamma} \dot{K} - \beta_K \right)$.

As a consequence, it is derived as

$$\begin{aligned}
\dot{V} &< -\beta_s \|\mathbf{s}\|_2 - \beta_K |K - K^*| - \kappa \\
&= -\beta_s \cdot \frac{\sqrt{2}}{\lambda_{max}^{1/2}} \cdot \frac{\lambda_{max}^{1/2}}{\sqrt{2}} \\
&\quad - \beta_K \cdot \sqrt{2\gamma} \cdot \frac{1}{\sqrt{2\gamma}} |K - K^*| - \kappa \\
&\leq -\sqrt{2} \min \left(\frac{\beta_s}{\lambda_{max}^{1/2}}, \beta_K \sqrt{\gamma} \right) \\
&\quad \cdot \left(\frac{1}{\sqrt{2}} \lambda_{max}^{1/2} \|\mathbf{s}\|_2 + \frac{1}{\sqrt{2\gamma}} |K - K^*| \right) - \kappa \\
&\leq -\beta \cdot V^{1/2} - \kappa
\end{aligned} \tag{84}$$

where $\beta \triangleq \sqrt{2} \min \left(\frac{\beta_s}{\lambda_{max}^{1/2}}, \beta_K \sqrt{\gamma} \right) > 0$.

The positiveness of parameter κ suggests that the γ must be selected properly. If $\kappa > 0$, it yields

$$\frac{1}{\gamma} \dot{K} - \beta_K > 0 \Rightarrow \gamma < \frac{\dot{K}}{\beta_K} \tag{85}$$

The adaptive law (38) is substituted and it derives as

$$\gamma < \eta \frac{K \left(\frac{\|\mathbf{s}\|_2}{\varepsilon} - 1 \right) + K_0}{\beta_K} = \Gamma(t) \tag{86}$$

The adaptive gain has a lower bound as $K(t) \geq K_0$ and if the region $\|\mathbf{s}\|_2 > \varepsilon$ is assumed, then

$$\eta \frac{K_0}{\beta_K} < \eta \frac{K \left(\frac{\|\mathbf{s}\|_2}{\varepsilon} - 1 \right) + K_0}{\beta_K} < \Gamma \tag{87}$$

Therefore, parameter γ must be chosen as

$$\gamma < \eta \frac{K_0}{\beta_K}. \tag{88}$$

Equation (84) shows that the Lyapunov function satisfies $\dot{V} \leq -\beta \cdot V^{1/2} - \kappa < -\beta \cdot V^{1/2}$. The finite time convergence of the sliding surface in the region $\|\mathbf{s}\|_2 \leq \varepsilon$ is guaranteed by Lemma 2. ■

Lemma 4. *If the i th component of the attitude sliding variable is bounded into the region $|s_i(t)| \leq \varepsilon_i$, then the quaternion error is bounded as $|q_{ei}(t)| \leq Q_i$ for $i = 1, 2, 3$. Q_i is the unique solution of the equation $f(Q_i) = 0$, where $f(x)$ is defined in (58).*

Proof:

Let the Lyapunov function $V = \frac{1}{2}\mathbf{q}_{ev}^T\mathbf{q}_{ev}$, then its time derivative is obtained as

$$\begin{aligned}\dot{V} &= \mathbf{q}_{ev}^T\dot{\mathbf{q}}_{ev} \\ &= \frac{1}{2}\mathbf{q}_{ev}^T(q_{e4}\mathbf{I}_{3\times 3} + \mathbf{q}_{ev}^\times)\boldsymbol{\omega}_e \\ &\leq \frac{1}{2}\mathbf{q}_{ev}^T\boldsymbol{\omega}_e \\ &= \frac{1}{2}\sum_{i=1}^3\dot{V}_i\end{aligned}\quad (89)$$

where $\dot{V}_i = q_{ei}\omega_{ei}$. The bound of the sliding variable $|s_i| \leq \varepsilon_i$ leads to the inequality equation as

$$g(q_{ei}) \leq \omega_{ei} \leq f(q_{ei}) \quad (90)$$

where $f(x)$ and $g(x)$ are functions in (58) and (59). Since $f(x)$ and $g(x)$ are the same with (58) and (59) of Lemma 3, the uniqueness of the solution for the equations $f(Q_{i,p}) = 0$ and $g(Q_{i,n}) = 0$ and their relationship $Q_{i,p} = -Q_{i,n} = Q_i$ are proven in the same way. Therefore, the region of attraction $\mathbb{L}_2 = \{q_{ei} \in \mathbb{R} \mid |q_{ei}| \leq Q_i\}$ derives that \dot{V} is negative when $|q_{ei}| > Q_i$ ■

V. Numerical Simulation

The orbital perturbations induce the external disturbance force in space. The Earth's geopotential model JGM3 determines the aspherical gravity by degrees and order of 70. The third-body gravity from the Sun and Moon are applied and treated as point masses. The gravity gradient torque from the point-mass Earth's gravity exerts a disturbance on the attitude control system. The residual dipole moment of 10^{-3} Am^2 in a random direction and the Earth's magnetic field of international geomagnetic reference field (IGRF) model generates magnetic disturbance torque. The atmospheric drag and solar radiation pressure are the common disturbances for the relative orbit control and attitude systems. The atmospheric density is calculated from the exponential model, and the solar radiation pressure adopts the constant solar flux. The internal uncertainties on the deputy satellite originate from the mass and moment of inertia. The uncertainties betide from the measurement errors. The non-gaussian random errors demonstrate these uncertainties for the software simulation.

The ROCS and ACS operate in closed loops inter-dependently. Fig.5 depicts the block diagram of both systems. The software algorithm of the ROCS, the orbit controller box, provides the relative orbit error states as inputs and generates the reference control input $\mathbf{u}_{orb,r}$. Let the reference control input from the control algorithm be denoted $\mathbf{u}_{orb,0}^l$ that corresponds to the one in the equation and the simulation result. The superscript indicates the variable's frame as section 2, and the subscript 0 is a temporary number of the process. The zero-order hold function holds the reference control input constant for the sampling time $T_{s,orb}$. The sampling time for the ROCS

system should be proper for both attitude control and immediate update of control input. $T_{s,orb}$ is 5 seconds in this simulation. The discretized signal $\mathbf{u}_{orb,1}^l$ is then converted to the body frame as $\mathbf{u}_{orb,1}^b$ to give an input to the orbital actuator, the propulsion system.

The resolution and the saturation limit of thrust firing and the restricted degrees of freedom contribute to the thrust error and produce $\mathbf{u}_{orb,2}^b$. In the numerical simulation, the fired thrust $\mathbf{u}_{orb,2}^b$ is converted to the $\mathbf{u}_{orb,2}^l$ and $\mathbf{u}_{orb,2}^i$, sequentially. Since the control algorithm utilizes the LVLH frame, the graphs in the simulation result analyze and compare $\mathbf{u}_{orb,2}^l$ which is the same as \mathbf{u}_{orb} . $\mathbf{u}_{orb,2}^i$ is the control input in the inertial frame and integrated with the orbital perturbations and mass uncertainties. The numerical integrator, ode45 of MATLAB provides the orbital states with every time step 0.01 seconds.

The ACS generates the reference attitude from the zero-ordered thrust vector in the body frame $\mathbf{u}_{orb,1}^b$ that is transmitted to ACS every orbital sampling time. Since the reference attitude possibly alters every orbital sampling time, the ACS should be able to converge the sliding variable within $T_{s,orb}$. Therefore, the orbital sampling time is critical for the attitude control performance. The attitude control problem of the time limit $T_{s,orb}$ repeats for the whole simulation duration. The reference torque is integrated with the disturbance torques and MoI uncertainties by the attitude dynamics with reaction wheels. The numerical integrator and the time step for the ACS system are the same as the one for the ROCS.

The procedure to search for the proper control parameters is as follows. The parameters that constitute the sliding variable are ρ , α and β . The parameter ρ determines the convergence rate of the nonsingular fast terminal sliding variable when it retains zero. The simple mathematics deduct that if $|x| < 1$ for an arbitrary variable x , x achieves zero much faster as ρ is smaller. Oppositely when $1 < |x|$, larger ρ shows faster convergence. Since the initial relative position error is likely to be larger than one meter and the definition of the quaternion restricts the initial quaternion error below one, it is recommended that ρ_{orb} and ρ_{att} are selected as 1.90 and 1.10, respectively. α and β attach weights to the error state relative to its time derivatives.

The three elements α_i for $i = 1, 2, 3$ are rated equally and the same for β_i for $i = 1, 2, 3$. As α and β become sufficiently large, it mitigates the direct influence from the control input to the relative velocity or the angular velocity, and the controlled states suffer less from the sudden rises. In this context, one of the parameters from the adaptive control law ε addresses related to the sliding variable. The control objective to bound the sliding variable below ε gives the critical importance to ε . A smaller value of ε implies a more accurate error in the steady state and a higher possibility for the actuator to be saturated for the same values of α and β . Several simulations and intuition help with the empirical tuning of those values.

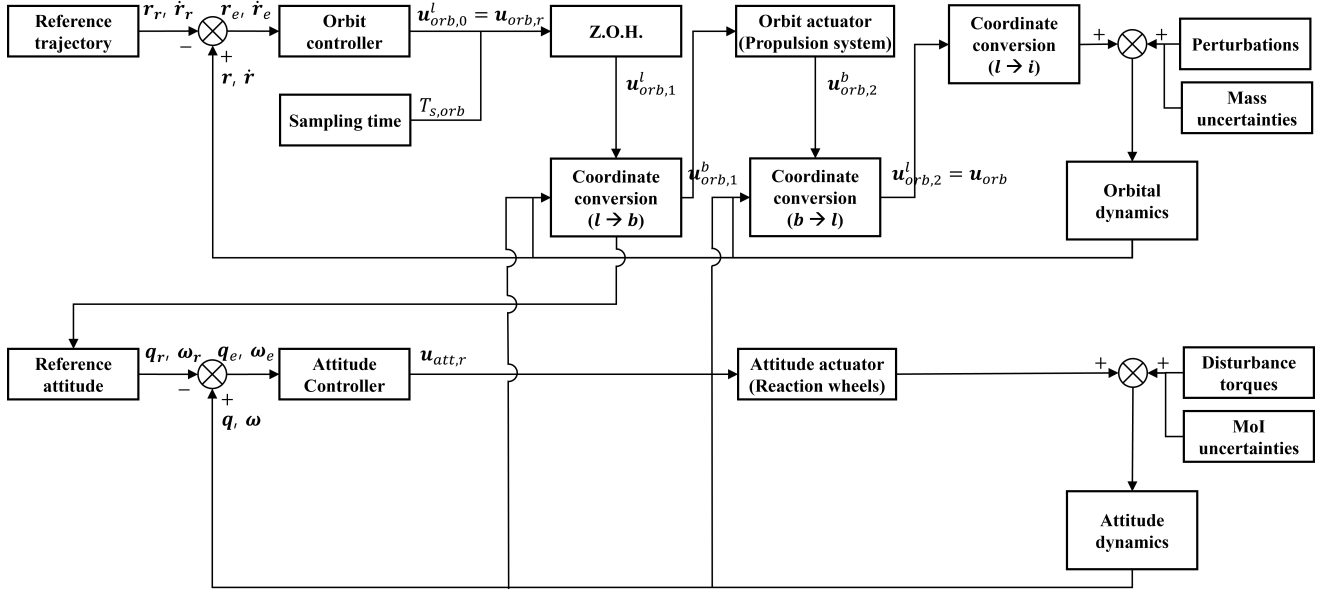


Fig. 5. Block diagram of control loops in formation flying system

The adaptive control law has the advantage of only a few parameters. Suppose that the sliding variable approaches the vicinity of ε to have the same order of ε . Then the control gain $K(t)$ has the same order as the control input u . Since the error is disposed to decrease, the initial control gain $K(0)$ could be chosen considering the actuator limit. The reorganized formula of the adaptive law in (91) suggests that the relative magnitude of $\|s\|_2 / \varepsilon$ and $\left(1 - \frac{K_0}{K(t)}\right)$ decides the sign of \dot{K} .

$$\dot{K}(t) = \eta K(t) \left(\left\| -\frac{s}{\varepsilon} \right\|_2 - \left(1 - \frac{K_0}{K(t)}\right) \right) \quad (91)$$

Therefore, K_0 and η affects how sensitively the sign and magnitude of \dot{K} fluctuate. In the same manner as other parameters, it needs a number of simulations and intuition.

Since $\alpha_{att,i}$ for $i = 1, 2, 3$ are set as the same, let $\alpha_{att} = \alpha_{att,i=1,2,3}$ is defined. β_{att} , α_{orb} , and β_{orb} are defined in the same way. If α_{att} , β_{att} , ρ_{att} , α_{orb} , β_{orb} and ρ_{orb} are set as 1.44, 1.44, 1.10, 7.00×10^{-3} , 7.00×10^{-3} and 1.90 for $i = 1, 2, 3$, then the error and its time derivative have the same order. ε_{att} and ε_{orb} are respectively set as 6.00×10^{-2} and 1.20×10^{-2} , considering the requirements in error and the control input saturation. The control parameters η_{att} , $K_{att}(0)$, $K_{att,0}$, η_{orb} , $K_{orb}(0)$ and $K_{orb,0}$ are 5.00×10^{-2} , 2.00×10^{-4} , 2.00×10^{-7} , 3.00×10^{-4} , 3.00×10^{-5} and 1.00×10^{-8} . These parameters are summarized in table I.

According to the top panel of Fig. 6, the two-norm of the orbital sliding variable rapidly decreases within 50 seconds, and initially converges below ε_{orb} at 330-365 seconds. It stays in the region ε_{orb} after 430 seconds. Even though the sliding variable temporarily exceeds ε_{orb} during 415-430 seconds, the appropriate choice of α_{orb} and β_{orb} holds the two norm of the position errors below

3 meters. The two-norm of the position error suggested in the middle panel of Fig. 6 initially reduces below the requirement at 41.36 seconds, and then remains in the region thereafter.

The position errors in each direction of the LVLH frame are described at the bottom panel. The radial position error stays at $-\sqrt{3}$ meters once it is stabilized. The along-track and cross-track position errors reach zero at about 400 seconds when the sliding variable converges. The along-track position error slowly increases to $\sqrt{3}$ at the end of the simulation. On the other hand, the cross-track position error remains near zero thereafter.

The reference thrust from the control algorithm $u_{orb,r}$ and the fired thrust u_{orb} has the thrust error $u_{orb,e}$ as mentioned in Fig.5, where $u_{orb,e} = u_{orb} - u_{orb,r}$. The fired thrust and the thrust error are depicted in top three panels of Fig. 7. The radial thrust error in the first panel has a positive value and rapidly decreases during the first 50 seconds. The positive thrust error suggests that the reference thrust is negative and controls the positive orbital error. It also explains the positive along-track and cross-track thrust errors in the second and third panels.

TABLE I

Simulation parameters for attitude and orbit control systems

ρ_{att}	α_{att}	β_{att}	ε_{att}
1.10	1.44	1.44	6.00×10^{-2}
$K_{att}(0)$	$K_{att,0}$	η_{att}	
2.00×10^{-4}	2.00×10^{-7}	5.00×10^{-2}	
ρ_{orb}	α_{orb}	β_{orb}	ε_{orb}
1.90	7.00×10^{-3}	7.00×10^{-3}	1.20×10^{-2}
$K_{orb}(0)$	$K_{orb,0}$	η_{orb}	
3.00×10^{-5}	1.00×10^{-8}	3.00×10^{-4}	

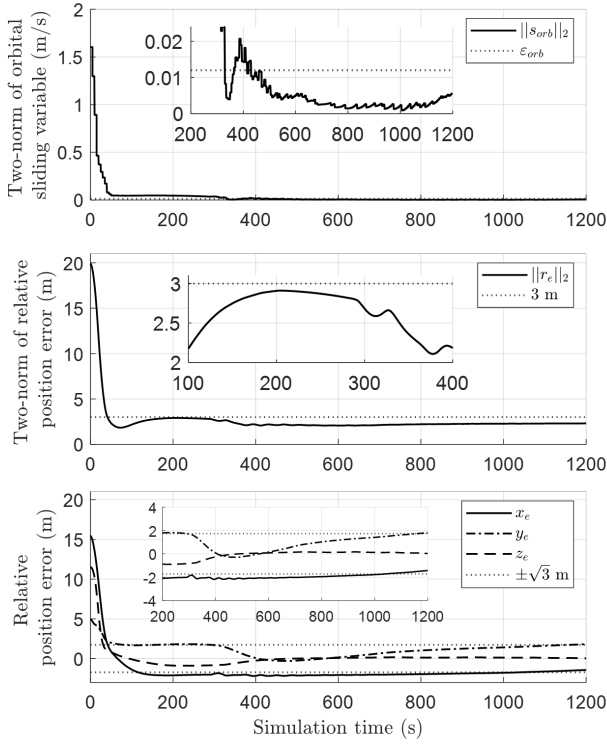


Fig. 6. Two-norm of the orbital sliding variable and position error

After 50 seconds, the magnitude of thrust is almost zero and induces the offset of the radial position error. After the convergence of the sliding variable, only a small magnitude of thrust is fired discontinuously. Because the propulsion system has a thrust resolution of 0.01 mN, the thrust could be fired once the reference thrust is large enough. Compared to the radial and along-track thrusts, the cross-track thrust easily controls the position error and consumes less fuel after the convergence. The fourth and fifth panels in Fig. 7 depict \dot{K} and K . According to the adaptation law in (91), the negative sign of \dot{K} and the converged K indicate that the sliding variable is bounded after 430 seconds.

The abrupt rises in the sliding variable and quaternion errors occur when the reference quaternion changes. According to the simulation result shown in Fig. 8, the two reference quaternions switch 32 times for 1200 seconds. The expectable reference quaternions make it possible to predict the convergence speed of the attitude sliding variable. The initial attitude is usually oriented far from the reference attitude in the beginning. The top two panels in Fig. 8 show that the change in the reference attitude could instantly reduce the control error during the first 50 seconds. The ROCS generates the reference thrusts more frequently before the orbital sliding mode converges at 430 seconds. The attitude maneuver is very regular and the convergence speed of the attitude sliding variable should be analyzed after 430 seconds. The attitude sliding variable is bounded by $\|s\|_2 \leq \varepsilon_{att}$ within 7.98 seconds

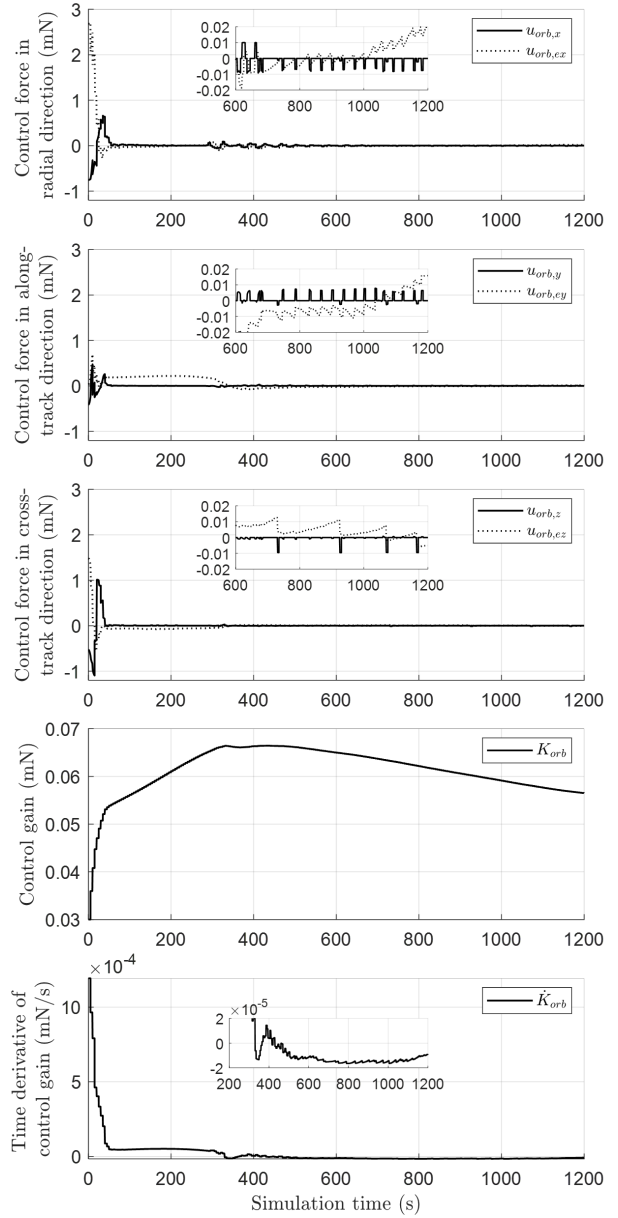


Fig. 7. Fired thrust, thrust error, orbital control gain and its time derivative

on average after 430 seconds including 38.20 seconds at the last control.

As it is described in Section II, the reference attitude rotates ± 10 deg along the $+\hat{b}_x$ axis to achieve the controllability in $+\hat{b}_z$ axis. Therefore, only the q_{e1} in the second panel momentarily increases except for the initial 50 seconds. Since the three components of the quaternion vector are coupled by the cross term in (23), the increase in q_{e1} causes q_{e2} and q_{e3} to fluctuate (the third and fourth panels).

The control torque profile in the top three panels in Fig. 9 corresponds to the trends of the quaternion errors. $u_{att,1}$ is temporarily saturated for about 10 seconds when the q_{e1} is at the peak. $u_{att,2}$ and $u_{att,3}$ are relatively small but never zero unless the three components in quaternion

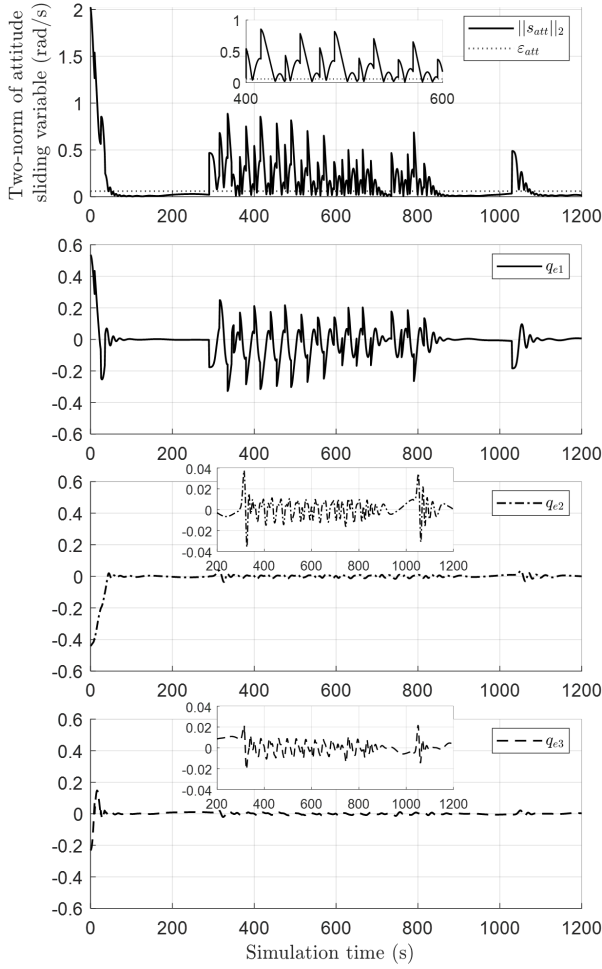


Fig. 8. Two-norm of the attitude sliding variable and quaternion error

error vectors become zero simultaneously. The fourth and fifth panels explain the rationale that the last convergence speed of the attitude sliding variable is latent. The attitude sliding variable stays in the region below ε_{att} for about 200 seconds before the last control (top panel of Fig. 8). Theoretically, \dot{K} is negative when $\|s\|_2 \leq \left(1 - \frac{K_0}{K}\right) \cdot \varepsilon_{att}$ and the simulation verifies that they are only 0.12 seconds different. Hence, \dot{K} is negative for considerable time and it provokes the significant reduction of K in the fourth panel.

The time allocation for the alignment in this mission is 20 minutes. According to the table II, this NFTSM control algorithm satisfies the mission requirement for 19.31 minutes and consumes 5.70 Ns of fuel. On the other hand, the linear quadratic regulator and PD control algorithm are embedded on board for ROCS and ACS, respectively. The Q and R matrices for the LQR controller are $Q = \text{diag}\{2.52 \times 10^{-3}, 2.52 \times 10^{-3}, 2.52 \times 10^{-3}, 1.04, 1.04, 1.04\}$ and $R = \text{diag}\{1.16 \times 10^4, 1.16 \times 10^4\}$. These algorithms retain the satellite within the requirement only for 3.18 minutes while it consumes 1.50 Ns. Therefore, the NFTSM control algorithm

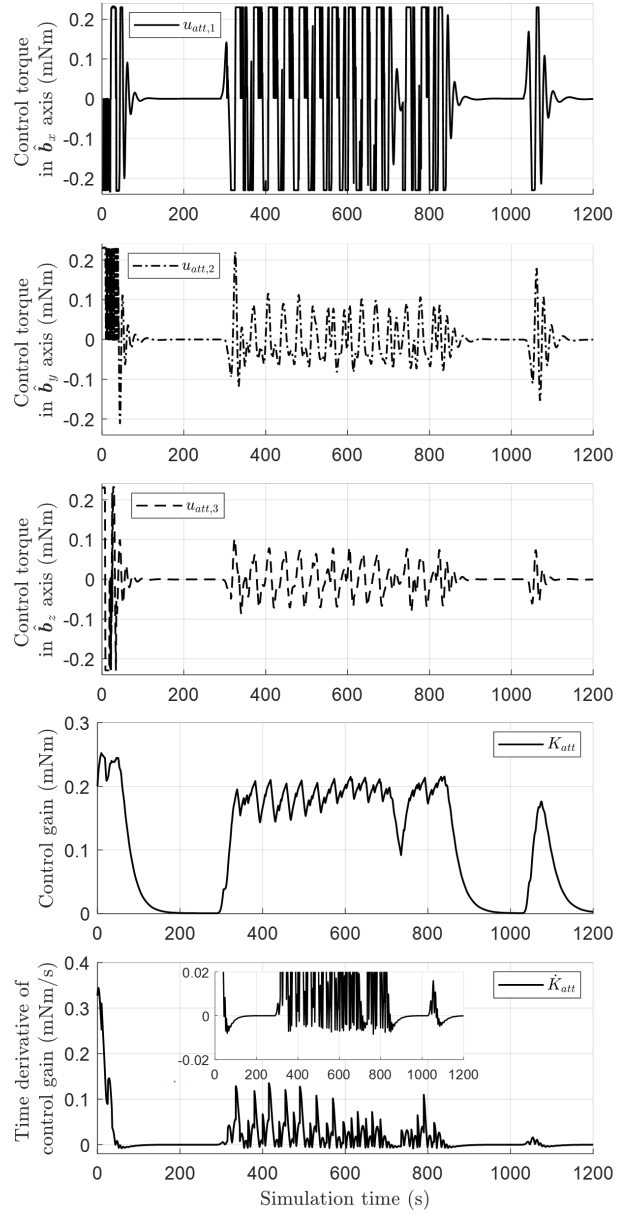


Fig. 9. Control torque, attitude control gain and its time derivative

extends the aligned time by 6.07 times and improves the fuel efficiency by 26.31 times.

VI. Conclusion

The virtual telescope demonstration mission requires precise control performance in both attitude and relative orbit control systems. Since the propulsion system has

TABLE II
Comparison of control algorithms

ROCS	ACS	Aligned time	Fuel consumption
LQR	PD	3.18 min	1.50 Ns
NFTSM	NFTSM	19.31 min	5.70×10^{-2} Ns

only two degrees of freedom, the attitude control performance could degrade the mission success possibility. In this paper, the nonsingular fast terminal sliding surface and the adaptive smooth controller are introduced to the attitude and relative orbit control system. The nonsingular fast terminal sliding mode naturally has a fast convergence rate and improves the aligned time. The control law is designed to have continuous signals and prevents the system from chattering—the radical problem of the classical sliding mode. The adaptive rule designed based on the vector norm of the sliding variable is able to consider the changes in the sliding variable. The simulation results show that the adaptive smooth controller based on the nonsingular fast terminal sliding mode dramatically improves the control performance with reasonable thrust consumption.

ACKNOWLEDGMENT

This research was supported by the Challengeable Future Defense Technology Research and Development Program through the Agency For Defense Development(ADD) funded by the Defense Acquisition Program Administration(DAPA) in 2023(No.915027201)

REFERENCES

[1] M. D'Errico Distributed Space Missions for Earth System Monitoring *Springer Science+Business Media New York*, 2013

[2] F. Kamalabadi, E. Lightsey, D. Rabin, A. Daw, S. D'Amico, A. Koenig, P. Chamberlin, T. Woods, S. Gupta, E. Ekici, J. Sample, H. Park, A. Alexeenko, J. Hwang, K. Denis, J. Klimchuk Distributed Space Telescopes Enabled by Constellation of Small Satellites *AGU Fall Meeting 2021, held in New Orleans, LA*, 13-17 December 2021

[3] B. A. Corbin The Values Proposition of Distributed Satellite Systems for Space Science Missions *Ph.D Thesis*, Department of Aeronautics and Astronautics, Massachusetts Institute of Technology, 2015

[4] B. D. Tapley, S. Bettadpur, M. M. Watkins, and C. Reigber The gravity recovery and climate experiment: Mission overview and early results *Geophysical Research Letters*, vol.31, no.9, May 2004, doi: [10.1029/2004GL019920](https://doi.org/10.1029/2004GL019920)

[5] R. P. Kornfeld, B. W. Arnold, M. A. Gross, N. T. Dahya, W. M. Klipstein, P. F. Gath, and S. Bettadpur GRACE-FO: The Gravity Recovery and Climate Experiment Follow-On Mission *Journal of Spacecraft and Rockets*, vol.56, no.3, May 2019, doi: [10.2514/1.A34326](https://doi.org/10.2514/1.A34326)

[6] A. Moreira, G. Kireger, I. Hajnsek, D. Hounam, M. Werner, S. Riegger, and E. Settelmeier TanDEM-X: A TerraSAR-X Add-On Satellite for Single-Pass SAR interferometry *Geosci. and remote Sens. Symp.* 2, 2004, doi: [10.1109/IGARSS.2004.1368578](https://doi.org/10.1109/IGARSS.2004.1368578)

[7] N. H. Roth Navigation and Control Design for the CanX-4/-5 Satellite Formation Flying Mission *M.S. Thesis*, University of Toronto, Toronto, Canada, 2011

[8] G. Bonin, N. Roth, S. Armitage, J. Newman, B. Risi, and R. E. Zee CanX-4 and CanX-5 Precision Formation Flight: Mission Accomplished! *29th Annual AIAA/USU Conference on Small Satellites*, pp.1–15, 2015

[9] C.W.T. Roscoe, J.J. Westphal, and E. Mosleh Overview and GNC design of the CubeSat Proximity Operations Demonstration (CPOD) mission *Acta Astronaut.*, vol.153, pp.410–421, 2018 doi: [10.1016/j.actaastro.2018.03.033](https://doi.org/10.1016/j.actaastro.2018.03.033)

[10] A. W. Koenig, B. Macintosh and S. D'Amico Formation Design of Distributed Telescopes in Earth Orbit for Astrophysics Applications

Journal of Spacecraft and Rockets, vol.56, no.5, Sep-Oct. 2019, doi: [10.2514/1.A34420](https://doi.org/10.2514/1.A34420)

[11] P. C. Calhoun, A.-M. Novo-Gradac, and N. Shah Spacecraft alignment determination and control for dual spacecraft precision formation flying *Acta Astronaut.*, vol.153, pp.349–356, 2018 doi: [10.1016/j.actaastro.2018.02.021](https://doi.org/10.1016/j.actaastro.2018.02.021)

[12] Air Force Research Inst. Technology Horizons: A Vision for Air Force Science and Technology 2010-30 AF/ST-TR-10-01-PR, Maxwell AFB, AL, Air Univ. Press, 2010.

[13] G.K. Skinner, Z. Arzoumanian, W.C. Cash, N. Gehrels, K.C. Gendreau, P. Gorenstein, J.F. Krizmanic, M.C. Miller, J.D. Phillips, R.D. Reasenberg, C.S. Reynolds, R.M. Sambruna, R.E. Streitmatter and D.L. Windt The Milli-Arc-Second Structure Imager, MASSIM: A new concept for a high angular resolution x-ray telescope *Proc. SPIE 7011*, 70110T-1-11, 2008, doi: [10.1117/12.789568](https://doi.org/10.1117/12.789568)

[14] W. Cash, P. Oakley, M. Turnbull, T. Glassman, A. Lo, R. Polidan, S. Kilston and C. Noecker The New Worlds Observer: scientific and technical advantages of external occulters *Proc. of SPIE 7010*, 70101Q-1-9, 2008 doi: [10.1117/12.789717](https://doi.org/10.1117/12.789717)

[15] L. Philippe, D. Luc, V. Sebastien and Z. Andrei ASPICS: a giant coronagraph for the ESA/ PROBA-3 formation flying mission *Proc. of SPIE 7731*, 773118-1-12, 2010, doi: [10.1117/12.858247](https://doi.org/10.1117/12.858247)

[16] B. R. Dennis, G. K. Skinner, M. J. Li, A. Y. Shih Very High-Resolution Solar X-Ray Imaging Using Diffractive Optics *Sol. Phys.*, vol. 279, pp.573–588, 2012, doi: [10.1007/s11207-012-0016-7](https://doi.org/10.1007/s11207-012-0016-7)

[17] J.-J. E. Slotine, and W. Li Applied Nonlinear Control *Pearson*, 1991

[18] V.I. Utkin Sliding Modes in Control and Optimization *Springer-Verlag Berlin, Heidelberg*, 1992

[19] Y. Shtessel, C. Edwards, L. Fridman, and A. Levant Sliding Mode Control and Observation *Springer New York Heidelberg Dordrecht London*, 2010

[20] C. Edwards and S. Spurgeon Sliding Mode Control: Theory and Applications *CRC Press*, 1998

[21] Godard and K. D. Kumar Fault Tolerant Reconfigurable Satellite Formations Using Adaptive Variable Structure Techniques *Journal of Guidance, Control, and Dynamics*, vol. 33, no. 3, pp. 969–984, May-June 2010

[22] T. Massey and Y. Shtessel Continuous Traditional and High-Order Sliding Modes for Satellite Formation Control *Journal of Guidance, Control, and Dynamics*, vol.28, no.4, pp.826–831, 2005

[23] R. R. Nair, L. Behera, V. Kumar and M. Jamshidi Multisatellite Formation Control for Remote Sensing Applications Using Artificial Potential Field and Adaptive Fuzzy Sliding Mode Control *IEEE Systems Journal*, vol. 9, no. 2, pp. 508–518, June 2015

[24] J. Zhou, Q. Hu and M. I. Friswell Decentralized Finite Time Attitude Synchronization Control of Satellite Formation Flying *Journal of Guidance, Control, and Dynamics*, vol.36, no.1 pp.185–195, 2013.

[25] G. Zeng and M. Hu Finite-time control for electromagnetic satellite formations *Acta Astronautica*, vol.74, pp.120–130, 2012.

[26] M. AlandiHallaj and N. Assadian Sliding mode control of electromagnetic tethered satellite formation *Advances in Space Research*, vol. 58, pp. 619–634, 2016

[27] J.-P. Park, S.-Y. Park, Y. Song, G.-N. Kim, K. Lee, H.J. Oh, J.-C. Yim, E.J. Lee, S.-H. Hwang, S.W. Kim, K.Y. Choi, D.S. Lee, S.H. Kwon, M.-S. Kim, S.-W. Yeo, T.-H. Kim, S.-H. Lee, K.B. Lee, J.-W. Seo, W.-H. Cho, J. Lee, J.-H. Park, Y.W. Kim, S.J. Kang, J. Hwang, S.H. Lee, J.-H. Yang, S. Jin CubeSat Development for CANYVAL-X Mission *14th International Conferences on Space Operations*, 2016, pp.681–691. doi: [10.5140/JASS.2019.36.4.235](https://doi.org/10.5140/JASS.2019.36.4.235).

[28] G.-N. Kim, S.-Y. Park, T. Lee, D.-E. Kang, S. Jeon, J. Son, N. Kim, Y.-K. Park, Y. Song, Development of CubeSat systems in formation flying for the solar science demonstration: The CANYVAL-C mission *Advances in Space Research*, vol.68, no.11, pp. 4434-4455, 2021 doi: [10.1016/j.asr.2021.09.021](https://doi.org/10.1016/j.asr.2021.09.021).

[29] H. D. Black A passive system for determining the attitude of a satellite *AIAA Journal*, vol.2, no.7, pp.1350–1351, 1964

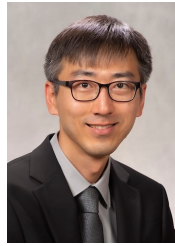
[30] J. R. Wertz *Spacecraft Attitude Determination and Control*

- [31] B. Wie *Space Vehicle Dynamics and Control, 2nd Ed.* Reston, VA, USA: American Institute of Aeronautics and Astronautics, Inc., 2008.
- [32] P. C. Hughes *Space Attitude Dynamics* John Wiley & Sons, 1986
- [33] K. T. Alfriend, S. R. Vadali, P. Gurfill, J. P. How and L. S. Breger *Spacecraft Formation Flying: Dynamics, control and navigation.* Burlington, MA, USA: Elsevier, 2010.
- [34] W. E. Wiesel *Spacecraft Dynamics, 2nd Ed.* McGraw-Hill, 1997
- [35] P. M. Tiwari, S. Janardhanan and M. Nabi Rigid spacecraft attitude control using adaptive integral second order sliding mode *Aerospace Science and Technology*, vol. 42, pp. 50–57, Jan. 2015, doi: [10.1016/j.ast.2014.11.017](https://doi.org/10.1016/j.ast.2014.11.017).
- [36] P. M. Tiwari, S. Janardhanan and M. Nabi Rigid Spacecraft Attitude Control Using Adaptive Non-singular Fast Terminal Sliding Mode *J. Control Autom. Electr. Syst.*, vol. 26, pp. 115–124, 2015, doi: [10.1007/s40313-014-0164-0](https://doi.org/10.1007/s40313-014-0164-0).
- [37] H. Cho, G. Kerschen and T. R. Oliveira Adaptive smooth control for nonlinear uncertain systems *Nonlinear Dyn.*, vol. 99, pp. 2819–2833, Jan. 2020, doi: [10.1007/s11071-019-05446-z](https://doi.org/10.1007/s11071-019-05446-z).
- [38] S. Yu, X. Yu, B. Shirinzadeh and Z. Man Continuous finite-time control for robotic manipulators with terminal sliding mode *Automatica*, vol. 41, no. 11, pp. 1957–1964, 2005, doi: [10.1016/j.automatica.2005.07.001](https://doi.org/10.1016/j.automatica.2005.07.001).
- [39] J. Wang and Z. Sun 6-DOF robust adaptive terminal sliding mode control for spacecraft formation flying *Acta Astronautica*, vol. 74, pp. 76–87, Dec. 2011, doi: [10.1016/j.actaastro.2011.12.005](https://doi.org/10.1016/j.actaastro.2011.12.005).
- [40] Z. Meng, W. Ren and Z. You Distributed finite-time attitude containment control for multiple rigid bodies *Automatica*, vol. 46, no. 12, pp. 2092–2099, Dec. 2010, doi: [10.1016/j.automatica.2010.09.005](https://doi.org/10.1016/j.automatica.2010.09.005).
- [41] S. P. Bhat and D. S. Bernstein Continuous Finite-Time Stabilization of the Translational and Rotational Double Integrators *IEEE Transactions on Automatic Control*, vol. 43 no. 5, pp. 678–682, May 1998, doi: [10.1109/9.668834](https://doi.org/10.1109/9.668834).
- [42] Y. Hong, J. Wang and D. Cheng Adaptive Finite-Time Control of Nonlinear Systems With Parametric Uncertainty *IEEE Transactions on Automatic Control*, vol. 51, no. 5, pp. 858–862, May 2006, doi: [10.1109/TAC.2006.875006](https://doi.org/10.1109/TAC.2006.875006).
- [43] Y. Tang Terminal sliding mode control for rigid robots *Automatica*, vol. 34, no. 1, pp. 51–56, Jan. 1998, doi: [10.1016/S0005-1098\(97\)00174-X](https://doi.org/10.1016/S0005-1098(97)00174-X).
- [44] Y.-J. Cheon Sliding Mode Control of Spacecraft with Actuator Dynamics *Transactions on Control, Automation, and Systems Engineering*, vol. 4, no. 2, Jun. 2022
- [45] K. Ma Comments on: Quasi-continuous higher order sliding-mode controllers for spacecraft-attitude-tracking maneuvers *IEEE Trans. Ind. Electron*, vol. 60, no. 7, pp. 2771–2773, 2013
- [46] S. Jeon, S.-Y. Park and G.-N. Kim Relative Orbit Control Algorithms and Scenarios for the Inertial Alignment Hold Demonstration Mission by CubeSat Formation Flying *Aerospace*, vol. 11, no.2, Feb. 2024, doi: [10.3390/aerospace11020135](https://doi.org/10.3390/aerospace11020135)
- [47] H. Kang Design and analysis of attitude system for CANYVAL-C cubesat mission *M.S. Thesis*, Yonsei university, South Korea, 2019



Soobin Jeon Soobin Jeon is a PhD candidate who will graduate in Aug 2024 at Yonsei University in South Korea. She received a B.S. degree in astronomy from the same university (2017). Her research field includes Guidance, Navigation, and Control (GN&C), robust control, and satellite constellation. She was involved in CubeSat missions such as CANYVAL-C and MIMAN and published a SCI(E) paper in Feb 2024. This paper addresses

another research interest, the robust control system development. She recently participated in the satellite constellation project and a KCI paper that dealt with the analytical orbit design of communication constellations with continuous coverage is accepted.



Hancheol Cho HANCHEOL CHO received the B.S. and M.S. degrees in astronomy from Yonsei University, Seoul, South Korea, in 2006 and 2008, and the Ph.D. degree in aerospace engineering from the University of Southern California, Los Angeles, CA, in 2012. From 2013 to 2015, he was senior research engineer with Samsung Techwin Co., Ltd. He was a Marie-Curie COFUND Postdoctoral Fellow with the University of Liege, Liege, Belgium

and a Postdoctoral Appointee with Sandia National Laboratories, Albuquerque, NM. From 2021 to 2023, he was an Assistant Professor with the Department of Aerospace Engineering, Embry-Riddle Aeronautical University, Daytona Beach, FL. Since August 2023, he has been an Associate Professor with the Department of Astronomy and the Department of Satellite Systems, Yonsei University, Seoul, South Korea. He also holds a visiting assistant professorship at Embry-Riddle Aeronautical University in Daytona Beach, FL. His research interests include spacecraft dynamics and control, robust adaptive controls, optimization, and robotics. He is an Associate Editor of the Journal of Control, Automation and Electrical Systems (Springer) and a member of the Astrodynamics Technical Committee of AIAA (American Institute of Aeronautics and Astronautics).



Sang-Young Park Dr. Sang-Young Park is a professor of the Astronomy Department as well as the Department of Satellite Systems at Yonsei University. He earned a Ph.D. degree in aerospace engineering from Texas A&M University in 1996. Since joining Yonsei in 2003, he has contributed to a variety of research fields in spacecraft dynamics and control, optimal control, orbit determination, spacecraft formation flying, and CubeSat systems.